POLITECNICO DI TORINO

Master Degree in Nanotechnologies for ICT's

Master's Degree Thesis

High-power gain-switched Ytterbium-doped fiber laser

Supervisors

Prof. Guido PERRONE

Prof.ssa Federica CAPPELLUTI

Prof.ssa Hanne LUDVIGSEN

Candidate

Beatrice Watty GAGLIANI

28th July 2020

Abstract

In the recent years intense studies have been focused on fiber lasers due to their intrinsic advantages as high beam quality, large wavelength tunability to robustness, and low cost. The development of its technology has been accomplished thanks to the evolution in fiber architectures and pumping schemes. In particular, Ytterbium-doped fibers have found great applications in the high-power laser systems in light of the idiosyncratic Ytterbium electronic structure.

This work presents a high-power fiber laser consisting of a gain-switched laser diode whose output pulses are amplified in a two-stage Ytterbium-doped polarization maintaining fiber amplifier [1]. The light source is simulated and experimental studied in order to assess its performance. Finally, the laser output is launched into a microstructured optical fiber which allows the supercontinuum generation owing to the combination of fiber dispersion and nonlinearities.

Acknowledgements

This work has been developed entirely at the department of Micro- and Nanosciences of the Aalto University in Finland. I would like to thank each person I have met in Micronova since they contribute in my professional formation. A special thank goes to my supervisor Hanne Ludgvisen who guides me along the fascinating world of optical fiber. I would also like to extend my gratitude to Steffen Novotny who was my advisor and helps me remotely during the post-lockdown. Thanks to my italian supervisor Guido Perrone for reassuring me and suggesting new working solutions despite the pandemic emergency. I cannot leave Micronova without mentioning Kuen Yao Lau who extended a great amount of assistance when I had to fix my broken setup.

I had great pleasure of meeting my international friends with whom I shared precious moments and I have to thank Finland for this opportunity.

I am deeply grateful to my parents and my friends Valentina, Flavia, Erminia and Antonella who, despite the distance, manage to stay by my side and fill me with their love.

Last but not least, thanks to Mattia who is not only the love of my life, but my mental anchor and closest confidant. Thank you to help me in believing in myself and remind me my skills when I am in a blue mood. My growth would have not been the same without your unwavering support and nurturing.

Letterarum radices amaras,
fructus dulces.

Table of Contents

List of Tables

List of Figures

Acronyms

MOF
Microstructured Optical Fiber

ZDW
Zero dispersion wavelength

NLSE
Non Linear Schrödinger Equation

SPM
Self-phase modulation

XPM
Cross-phase modulation

FWM
Four-wave mixing

SRS
Stimulated Raman Scattering

SBS
Stimulated Brillouin Scattering

MI
Modulation Instability

SC
Super Continuum

GS

Gain Switched

PML

Perfectly Matched Layer

FBG

Fiber Bragg Grating

PM

Polarization Maintaining

ASE

Amplified Spontaneous Emission

Chapter 1

Introduction

In the recent years many optical devices have been replaced by new architectures. In particular, fiber lasers have been the focus of intense researches due to their advantages spanning from high beam quality, large wavelength tunability to robustness and low cost [2].

Work on fiber lasers started at the Southampton University in England in 1985 by Sir David Payne and co-workers [3]-[4]. Subsequently, the need for even higher output power has pushed the scientific community towards the use of optical fibers doped with rare-earth elements such as ytterbium and thulium. The fiber technology has grown mature and can provide a platform for fabricating robust laser systems. The core and cladding structures can be tailored to control the beam shape, optical nonlinearities and scale-up the power. The power evolution in fiber lasers with near diffraction-limited output depends critically on the choice of the dopant of the active fiber as well as the pumping technologies. In this regard, the current-state-of-the-art makes an extensively use of Q-switched fiber lasers in the field of low-cost laser marking. Nevertheless, further improvements of peak output power, pulse duration and architecture are still on going. An attractive alternative to Q-switch fiber lasers are gain-switch fiber lasers, mainly attributed to the combination of a simple all-fiber geometry and an enhanced output with both good beam quality and high tunability.

Fiber lasers have found use in a wide range of applications including supercontinuum generation, wavelength conversion, industry, defense, automotive, security and medicine [5]. They are well-suited for interferometric applications as was demonstrated in *S. Novotny et al.* [1]. The authors utilized a gain-switched fiber laser to characterize vibration fields of electromechanical components up to GHz frequency. The footprint of this research is the use of a picosecond supercontinuum light source which stands out for its ultra-broad spectrum. In fact, since the output light of the fiber laser is coupled into a microstructured optical fiber, the generation of a high-bright light is possible thanks to the interplay between nonlinearities and

dispersion effects.
Several studies have been focusing on this phenomenon due to the combination of wide spectrum, high spectral power densities and high spatial coherence. Additionally, it is able to solve a shortcoming of conventional lasers which is the dependency of the emission wavelengths on the element suitable for lasing: a supercontinuum light source allows the selection of the desirable wavelength.

The objective of this thesis is to characterize the performance of the fiber laser used as supercontinuum light source developed in [1]. The work is organized as follows. Chapter 2 provides an overview of the different typologies of nonlinear phenomena including inelastic scattering processes and the optical Kerr effect. In Chapter 3 the basic and essential properties of microstructured optical fiber are presented. Successively, the mechanisms behind supercontinuum generation are briefly described. A comparison between Gain-switched and Q-switched mechanisms, a description of fiber laser architecture and the presentation of the experimental setup are reported in Chapter 4. Finally, the characterization and modelling of the fiber laser together with the assessment of the SCG performance are reported in Chapter 5.

Chapter 2

Nonlinearities

The interaction of electromagnetic radiation with polarized material leads to a wide range of nonlinear phenomena. This chapter briefly presents those relevant for the generation of supercontinua using picosecond pulses, such as optical Kerr effect, modulation instability, solitons, and inelastic scattering processes.

2.1 Light - matter interaction

When an intense electromagnetic field impinges on a dielectric material its response becomes nonlinear. Consequently, the dipole distribution can be written as

$$\vec{P} = \epsilon_0(\chi^{(1)}\vec{E} + \chi^{(2)}\vec{E}\vec{E} + \chi^{(3)}\vec{E}\vec{E}\vec{E}), \tag{2.1}$$

where ϵ_0 denotes the vacuum permettivity and $\chi^{(j)}$ (J = 1, 2, ...) is the j-th order susceptibility which is a tensor accounting for the light polarization. The first order susceptibility mainly contributes to the linear effect and the higher orders are responsible for nonlinear effects.
An optical fiber typically made of silica exhibits a symmetrical structure, and hence $\chi^{(2)}$ is zero. Therefore, the most relevant nonlinear effects are related to $\chi^{(3)}$. These nonlinear phenomena are listed in Table 2.1 and shown schematically in the diagram in Figure 2.1.

Table 2.1: *Nonlinear effects of* $\chi^{(3)}$.

Real part	**Imaginary part**
Kerr effect	Stimulated Raman Scattering
Self-phase modulation (SPM)	Stimulated Brillouin Scattering
Cross-phase modulation (XPM)	-
Four-wave mixing (FWM)	-

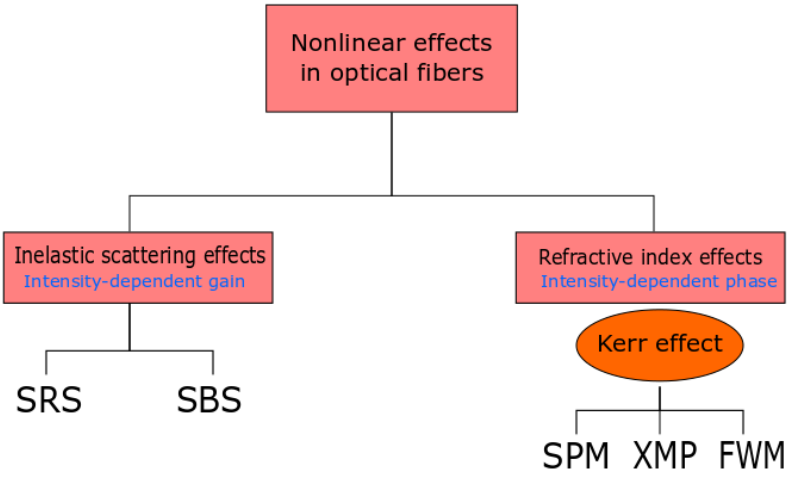

Figure 2.1: *Diagram of the fundamental nonlinear phenomena.*

For stronger fields, the nonlinear component of the dipole distribution can be written as

$$\vec{P_{NL}} = \epsilon_0 \chi^{(3)} \vdots \vec{E}\vec{E}\vec{E}. \tag{2.2}$$

After applying the Fourier transform and some mathematical computations [6], the refractive index in the frequency domain can be expressed as

$$\tilde{n}(\omega, |E|^2) = n(\omega) + n_2 |E|^2, \tag{2.3}$$

where $n_2 = \frac{3}{8n} Re(\chi^{(3)}_{xxxx})$ is the nonlinear refractive index and $|E|^2$ the field intensity.
For silica the value is $\approx 2.6 \cdot 10^{-20} m^2/W$ which appears to be almost negligible. However, in optical fiber the *core size* and the *fiber length* strongly enhance the nonlinear effect and can be observable at relatively low power. The strength of the nonlinearities can be estimated using the following three parameters.

- The **effective core area** is a quantitative measure of the area which a waveguide or fiber mode effectively covers in the transverse dimensions [7].

$$A_{eff} = \frac{(\int_{-\infty}^{+\infty} |E|^2 dA)^2}{\int_{-\infty}^{+\infty} |E|^4 dA} \tag{2.4}$$

  Assuming a Gaussian beam, the effective area is expressed by $A_{eff} = \pi w^2$, where w is the Gaussian width .

- The **effective length** is defined as the length along which the power can be considered constant
$$L_{eff} = \frac{1}{\alpha}[1 - exp(-\alpha L)]. \tag{2.5}$$
- Since the group velocity of a signal travelling into a fiber is frequency-dependent this caused **group velocity dispersion**, quantified by $\beta_2 = -\frac{\lambda}{2\pi c}(\frac{dn_g}{d\lambda})$, being n_g the group velocity index.

2.2 Optical Kerr effect

The material response to the incoming light is quantified by the refractive index. For small intensity it depends uniquely on the impinging frequency, in contrast if the input power increases and becomes strong the refractive index changes following Equation 2.3. The intensity-dependency of the refractive index is called *optical Kerr effect* and it is the cause of the phase variation during the wave propagation.

When a signal traveling in the fiber is considered, its evolution taking care of both nonlinearities and dispersion is described by the solution of the nonlinear Schrodinger equation (NLSE)

$$\frac{\partial A}{\partial z} + \beta_1 \frac{\partial A}{\partial t} + \frac{i}{2}\beta_2 \frac{\partial^2 A}{\partial t^2} = i\gamma |A|^2 A, \tag{2.6}$$

where β_1 and β_2 refer to dispersion, related to group velocity and group velocity dispersion (GVD) respectively, γ is the nonlinearity coefficient, A denotes the pulse amplitude and A_{eff} the effective core area.
The signal acquires a phase after propagating a distance L

$$\Phi = \beta L = k_0 \tilde{n} L = k_0 (n + n_2 I) L = \frac{2\pi}{\lambda}(n + \frac{n_2 P}{A_{eff}})L. \tag{2.7}$$

The phase is the sum of two contributions, a linear and a nonlinear phase, defined as $\phi_L = \frac{2\pi n L}{\lambda}$ and $\phi_{NL} = \frac{2\pi n_2 P L}{\lambda A_{eff}} = \gamma P L$, respectively.

Therefore, the phase change per unit length per unit power is given by the nonlinear parameter

$$\gamma = \frac{\omega_0 n_2}{c A_{eff}}. \tag{2.8}$$

The length scale over which nonlinear effects are not negligible is determined by the nonlinear length

$$L_{NL} = \frac{1}{\gamma P_0}. \tag{2.9}$$

When dispersion effects are included, the nonlinear length is compared to the dispersion length ($L_D = \frac{T_0^2}{|\beta_2|}$, where T_0 input pulse width) in order to find the

dominant effect for the pulse evolution. Depending on the nonlinear length, the material length and the dispersive length four different cases can be faced [8].

- $L << min(L_{NL}, L_D)$ Neither nonlinear nor dispersive effects are significant in the medium.
- $L_D \leq L << L_{NL}$ Dispersion is fundamental and nonlinearities can be neglected.
- $L_{NL} \leq L << L_D$ It is the complementary of the above case: nonlinearities play a dominant role whereas dispersion does not.
- $L \geq max(L_{NL}, L_D)$ both effects manifest along the medium length.

In conclusion, if chromatic dispersion induces distortion of the pulse shape then the Kerr effect modifies the spectrum. The intensity-dependence leads to the following most relevant effects: self-phase modulation, cross-phase modulation and four-wave mixing.

2.2.1 Self-phase modulation

While an optical pulse propagates in the fiber a self-induced nonlinear shift of the phase occurs due to the intensity-dependence of the phase.
Assuming a plan harmonic wave

$$E(t) = E_0(t)e^{-j(\omega t - \beta z)}, \tag{2.10}$$

where ω and β are the frequency and propagation constant, respectively, the Kerr effect induces a time-dependent phase shift $\phi(t)$ which can be written as

$$\phi(t) = \omega t - \beta z = \omega t - \frac{\omega}{c}[n + n_2 I(t)]z. \tag{2.11}$$

Although the initial pulse is unchirped, a temporal variation of the instantaneous frequency occurs after the propagation and accordingly, the signal broadens.
The temporal variation of the instantaneous frequency is

$$\omega(t) = \frac{d\phi(t)}{dt} = \omega - \frac{\omega}{c} n_2 z \frac{dI}{dt} = \omega - \delta\omega(t), \tag{2.12}$$

hence the frequency deviation due to nonlinearities is

$$\Delta\omega = \frac{d\phi_{NL}}{dt} = \gamma L \frac{dP}{dt}. \tag{2.13}$$

Since $\delta\omega$ is time-dependent the signal is chirped and according to the sign of its variation two cases can take place. For $\frac{dI}{dt} > 0$ the frequency decreases being red-shifted, while for $\frac{dI}{dt} < 0$ ω increases leading to a blue-shift.

The maximum phase shift is

$$\phi_{max} = \frac{z_{eff}}{L_{NL}} = \gamma P_0 z_{eff}, \tag{2.14}$$

where z_{eff} is the effective distance, if losses are neglected $z_{eff} = z$. Thus, the maximum phase is dependent on the peak power and for ultrashort pulses the broadening can be of the order of $100THz$. The maximum broadening associated to the phase shift is

$$\delta\omega_{max} = 0.86\Delta\omega\phi_{max}. \tag{2.15}$$

In addition, during the propagation of the pulse not only new frequencies are generated also the spectrum presents additional peaks. Their number is related to the maximum phase shift according to

$$\phi_{max} \approx (M - 0.5)\pi. \tag{2.16}$$

Figure 2.2 shows a Gaussian pulse propagating in a fiber and the broadening caused by the Kerr effect which generates new frequency. An oscillatory behaviour covers the entire spectrum which is explained by Figure 2.3. In fact, same chirp occurs for two opposite values of T which represent two waves with same frequencies and different phase; these two waves interfere both constructively and destructively leading to peaks present in the broadened spectrum.

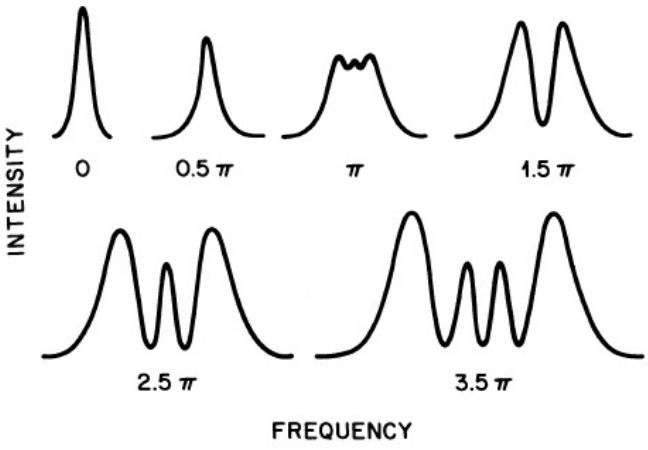

Figure 2.2: *SPM-broadened spectra for an unchirped Gaussian pulse. Designations referred to the maximum nonlinear phase shift [6].*

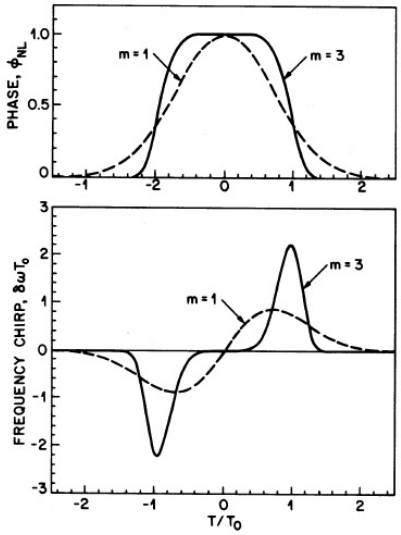

Figure 2.3: *Time dependence of SPM-induced phase shift (a) and frequency chirp (b) for a Gaussian beam [6]- [9].*

Despite all interesting properties are observed for chirped signals. From Figure 2.2, in correspondence of a large central region of the Gaussian beam the chirp is linear and positive. Moreover, the chirp is considerably larger for pulses with steeper leading and trailing edges as shown from the dashed and straight lines in Figure 2.3.

2.2.2 Cross-phase modulation

When two pulses travel along the fiber, the intensity of one pulse affects the nonlinear refractive index the other pulse. This causes a phase shift for both pulses and new frequencies generation.
The variation of nonlinear refractive index is given by

$$\Delta n_{NL} = n_2(|A_1|^2 + b|A_2|^2), \tag{2.17}$$

where $|A_1|^2$ and $|A_2|^2$ are the field intensities. The above expression accounts for the dependency of refractive index on both the intensity of the co-propagating waves.

In this case, the nonlinear phase shift is represented by

$$\phi_{NL} = \frac{4\pi L}{\lambda_i} n_2 |A_i|^2, \tag{2.18}$$

where A_j^2 are the field intensities and λ_i their wavelength, respectively. This parameter is known also cross-phase modulation and a temporal overlap between the two co-propagating fields is required to obtain it.

2.2.3 Four-wave mixing

When three waves of different frequencies co-propagate in the fiber, $\chi^{(3)}$ generates a forth field under the conservation of both energy and momentum.
In the quantum mechanical description, this happens when photons from one or more waves are annihilated and photons of different energies are generated [6]. Supposing to have three waves with frequency ω_1, ω_2 and ω_3 respectively, the total electric field is

$$\vec{E} = \hat{x}\frac{1}{2}\sum_{j=1}^{4} E_j exp[i(k_j z - \omega_j t)] + c.c. \tag{2.19}$$

The nonlinear polarization is computed as

$$\vec{P_{NL}} = \hat{x}\frac{1}{2}\sum_{j=1}^{4} P_j exp[i(k_j z - \omega_j t)] + c.c. \tag{2.20}$$

and for P_4 the following expression has been obtained

$$P_4 = \frac{3\epsilon_0}{4}\chi^{(3)}_{xxx}\{[I_4+2(I_1+I_2+I_3)]E_4+2E_1E_2E_3exp(i\theta_+)+2E_1E_2E_3^*exp(i\theta_-)+...\}, \tag{2.21}$$

where I_j are the field intensities and $\theta_{+/-}$ are defined as

$$\theta_+ = (k_1 + k_2 + k_3 - k_4)z - (\omega_1 + \omega_2 + \omega_3 - \omega_4)t, \tag{2.22}$$

$$\theta_- = (k_1 + k_2 - k_3 - k_4)z - (\omega_1 + \omega_2 - \omega_3 - \omega_4)t. \tag{2.23}$$

The term proportional to E_4 results in SPM and XPM, whereas the other terms are responsible of FWM.
The photon generated may belong to two different categories. On one side, all photons can transfer their energy to the single photon, obtaining a frequency of $\omega_4 = \omega_1 + \omega_2 + \omega_3$ which can generate either a third-harmonic (if $\omega_1 = \omega_2 = \omega_3$) or frequency conversion ($\omega_1 = \omega_2 \neq \omega_3$). On the other, two photons having frequency ω_1 and ω_2 respectively, can be annihilated generating two new photons ω_3 and ω_4. It must be noticed that in FWM process power transfer is required to obey to the energy conservation, contrarily in XPM this does not happen and only an asymmetrical spectral broadening is obtained.

For really high optical intensities the refractive index does not increase linearly with the intensity, indeed a saturation and even substantial decrease occur in some cases [10]. These are attributed to the multiphoton ionization which leads to further induced losses. The latter results in an additional phase changes via Kramers-Kronig relations [11] - [12].

2.2.4 Solitons

During the pulse propagation spectrum broadening can be attributed to both dispersion and nonlinear effects, as illustrated in Figure 2.4. When these effects coexist interesting phenomena can take place. Generally, if the system is in normal dispersion the nonlinear broadening will be further enhanced, while if in anomalous dispersion its effect can be compensated by nonlinear effects. If SPM is the dominant effect, a stabilized wave called **soliton** can be generated only when GDV balances the nonlinearity.
Solitons can be categorised in temporal and spatial waves. In the field of optics, and in particular in fibers, temporal solitons manifest when the electromagnetic field is confined in the waveguide and the pulse shape does not change in time due to the balance between nonlinear and dispersion effects. On the contrary, spatial solitons can propagate when the field is not spatial confined maintaining unaltered the pulse shape because of the interplay between nonlinearities and diffraction [13].

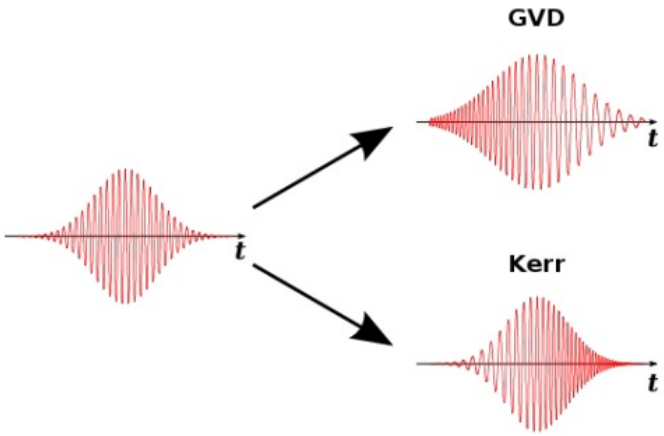

Figure 2.4: *Effects of dispersion (top) and nonlinearities (bottom) on a Gaussian pulse in the time domain [6].*

Since this work deals with fiber optics, only temporal solitons are considered. An useful parameter which defines the order of the soliton is expressed by

$$N^2 = \frac{L_D}{L_{NL}} = \frac{\gamma P_0 T_0}{|\beta_2|}. \tag{2.24}$$

For instance if $N = 1$ the soliton, called fundamental soliton, is represented by a relatively simple equation in which SPM and GVD are equally balanced. As shown in Figure 2.5, the equilibrium allows the wave propagation without distortion even

though interactions with other waves are present. This happens because in the anomalous region the chirp caused by GVD is negative, while the one induced by SPM is positive leading to a chirp-free environment. From simple computations [6], the peak power needed to create the fundamental soliton is

$$P_1 = \frac{|\beta_2|}{\gamma T_0^2} \tag{2.25}$$

instead, the soliton period is described by

$$z_0 = \pi/2 L_D = \pi/2 \frac{T_0^2}{|\beta_2|}. \tag{2.26}$$

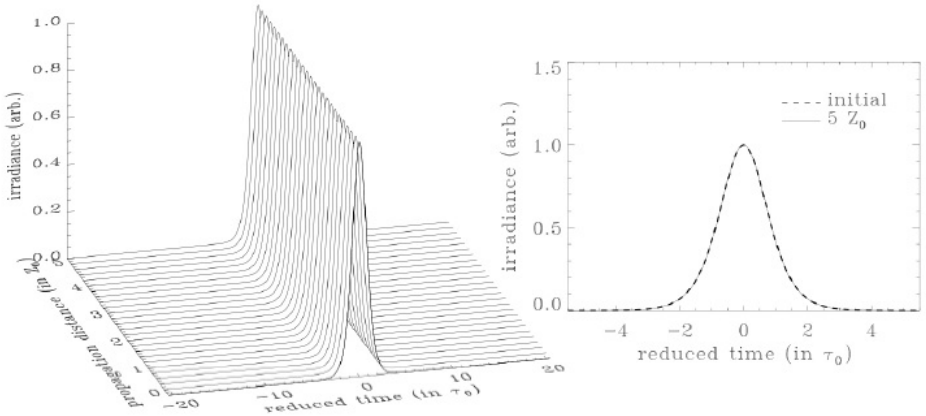

Figure 2.5: *Temporal soliton in a nonlinear and dispersive medium: after travelling 5 times the confocal distance its shape remains the same [13].*

For higher-order solitons at the initial time SPM dominates but then GVD contracts the pulse: the shape of the pulse changes periodically with a period $\xi_0 = \pi/2$. For example, if the soliton pulse period at $T_0 = 1ps$ is about 80 m, after 10 ps it reaches 8 km since it scales as T_0^2. Indeed, the maximum power needed to produce higher solitons scales as N^2, the propagation of such pulses could damage the medium [6].

Dispersive wave

When the perturbation induced by a higher-order dispersion causes the energy transfer from a soliton to a narrow band resonance a dispersive wave is generated. More in details, the higher-order solitons break into fundamental solitons (this

process is named soliton fission) and during the decay each wave emits a blue-shifted radiation at a wavelength depending on the phase-matching condition (see Appendix 5.1.2). In this way, the spectral broadening is initialized and a gap is formed in the vicinity of the ZDW. Finally, the gap is filled by a complex interaction between FWM and SRS, having as a final result a broad and flat spectrum. Additionally, dispersion has a huge contribution in the generation of dispersive wave: the normal dispersion condition is necessary for the rise of new spectral components. Although these waves are undesirable because they represent an energy loss and affect the performance of soliton in communication systems [14], it is one mechanism adopted for the generation of the supercontinuum in optical frequency metrology [15].

2.3 Modulation instability

For many nonlinear setups, the combined effect of dispersion and nonlinearities can lead to a sudden break up in time of the propagating signal. This phenomenon is known under the name of modulation instability of the steady state solution and can be observed in different physical fields. In the case of optical fiber, the continuous or semi-continuous wave is broken into a train of short-ultra pulses which propagate along the medium. Under anomalous condition, this process can lead to the generation of a broad spectrum.

Stability of optical solitons

Basing on the studies reported in [6], a CW solution of the Schrodinger nonlinear equation is considered. Its stability is checked by performing a linear stability analysis, which consists in inserting a small perturbation in the system. Two different cases can be faced:

- A *stable solution* in which perturbation creates a restoring action.
- On the contrary, the perturbation can grow in time generating an *unstable solution*.

If CW is considered its solution to Equation 2.6 in steady-state condition is

$$\tilde{A} = \sqrt{P_0} e^{i\phi_{NL}}, \tag{2.27}$$

where P_0 is the impinged power at z=0 and $\phi_{NL} = \gamma P_0 z$ the nonlinear phase shift.

After applying a small perturbation a, the solutions turns in

$$\tilde{A} = (\sqrt{P_0} + a) e^{i\phi_{NL}}, \tag{2.28}$$

which modifies Equation 2.6 in

$$i\frac{\partial a}{\partial z} = \frac{1}{2}\beta_2\frac{\partial^2 a}{\partial t^2} - \gamma P_0(a + a^*). \tag{2.29}$$

The latter could be easily solved in the frequency domain since it is linear in a. Unfortunately, the term a^* couples the Fourier components at $+\Omega$ and $-\Omega$ respectively, as a consequence the proposed solution turns to be in form

$$a(z,t) = a_1 exp[i(Kz - \Omega t)] + a_2 exp[-i(Kz - \Omega t)], \tag{2.30}$$

where K is the wave number and Ω the frequency of the perturbation. Equations 2.29 and 2.30 form a set of two homogeneous equations for both a_1 and a_2 which has nontrivial solution only if the following dispersion relation is satisfied

$$K = \pm|\beta_2\Omega|[\Omega^2 + sgn(\beta_2)\Omega_c^2]^{1/2}. \tag{2.31}$$

In the equation, $sgn(\beta_2) = \pm 1$ depends on both the dispersion sign and the expression below

$$\Omega_c^2 = \frac{a\gamma P_0}{|\beta_2|} = \frac{4}{|\beta_2|L_{NL}}. \tag{2.32}$$

The dispersion relation in Equation 2.31 clearly reports the dependency of the steady-state stability on the dispersion sign. In the case of normal dispersion, K is a real number for the entire range of frequencies which leads to a stable perturbation. On the contrary, in anomalous condition K is imaginary when $|\Omega| < \Omega_c$ and the perturbation exponentially grows and consequently the solution for Equation 2.27 is unstable. As previously anticipated, under these conditions modulation instability takes place inducing a spontaneous modulation in time of the beam and then the generation of a train pulses.

In Figure 2.6, the gain spectra of MI for three power levels is reported: two spectral sidebands are always simultaneously present which are represented mathematically in Equation 2.30 by the two terms at $\omega_0 \pm \Omega$. For this reason, the process can be equivalently interpreted as a FWM.

The gain is obtained when $|\Omega| < \Omega_c$ and its expression is

$$g(\Omega) = |\beta_2\Omega|(\Omega_c^2 - \Omega^2)^{1/2}. \tag{2.33}$$

As illustrated in Figure 2.6, for null frequency its value is zero, therefore it increases being symmetrical with respect to Ω and reaches the maxima of $g_{max} = 2\gamma P_0$ for $\Omega_{max} = \pm\frac{\Omega_c}{\sqrt{2}} = \pm\sqrt{\frac{2\gamma P_0}{|\beta_2|}}$. Notice that the peak value does not depend on the dispersion and it varies linearly with the incident power.

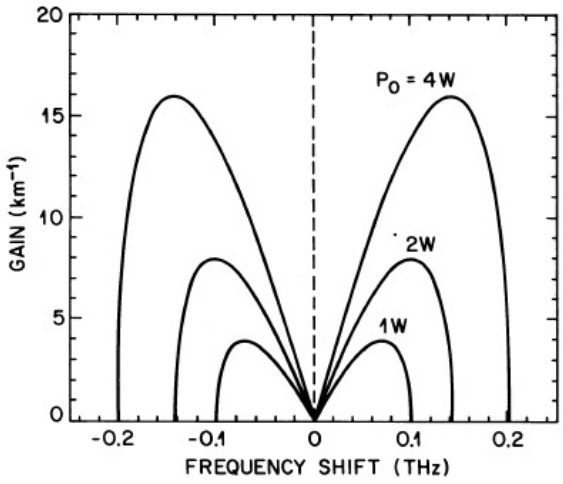

Figure 2.6: *Gain spectra for three input power [1] generated by Nd:YAG laser at* $\Delta\tau = 100ps$, $P_{av} = 7.1W$ *and* $L = 1km$ *and fiber paramenters* $\gamma = 2/(Wkm)$ *and* $\beta_2 = -20ps^2/km$ *[6].*

In this discussion the attenuation has been neglected, although it should be pointed out that MI is affected by losses. In particular if it is combined with nonlinearities and higher-order effects it leads to intrapulse Raman scattering and self-steepening. Reduction of the growth rate and gain range of frequency are side-effects of the latter.

2.4 Stimulated Raman scattering

In linear optics the low power intensity induces elastic scattering. When the collision takes place, the photon frequency remains unchanged and light can be either deflected or delayed, which leads to attenuation and dispersion. Conversely, at high light intensity the scattering becomes inelastic and cannot be formalized in a linear description. After the collision light changes both amplitude and phase, allowing for the generation of new frequencies and the achievement of gain.
The nonlinear scattering process, illustrated in Figure 2.7, is a multi-body interaction involving the molecule, photons and phonons, which are quanta of vibrational lattice. During the collision a phonon can be either emitted or absorbed, two processes known as Stokes and anti-Stokes scattering respectively. If the phonon is optical then a Raman scattering occurs whereas if it is acoustic the phenomenon is called Brillouin scattering.

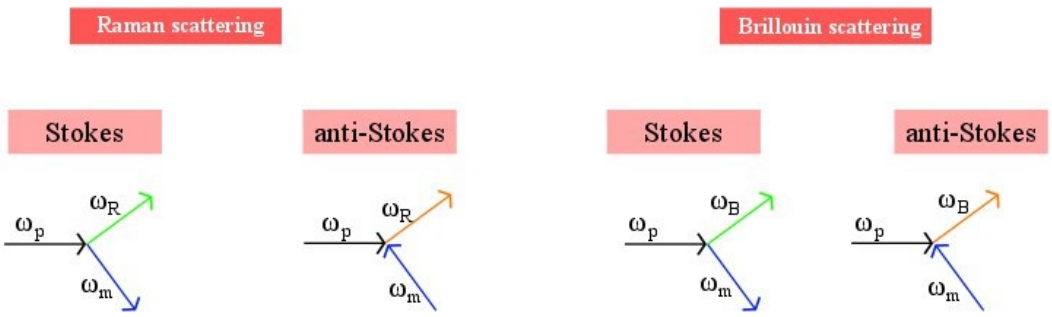

Figure 2.7: *Schematic overview of nonlinear scattering processes.*

In a microscopic description, after the scattering the system acquires enough energy to excite the molecule to a higher vibrational state, as shown in the band diagram sketched in Figure 2.8. Subsequently, a relaxation occurs which leads to the emission of a new photon with frequency $\omega = \omega_p \pm \omega_R$. It is fundamental to highlight that gain is obtained only for a stimulated process, hence the condition of phase matching is required. In this case one can deal with stimulated Raman and Brillouin scattering.

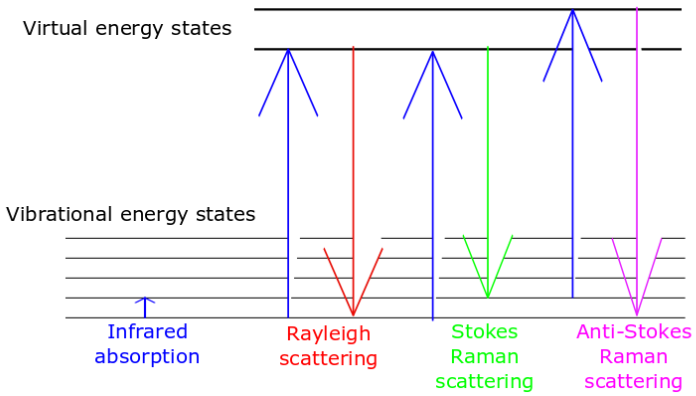

Figure 2.8: *Schematic overview of nonlinear scattering processes.*

Stimulated Raman Scattering

When the incident photon scatters with the molecule, the system allows a molecular transition between two vibrational states resulting in the emission of a new photon having lower frequency.
The process is governed by the following two coupled equations

$$\frac{dP_p}{dz} = -\alpha_p P_p - (\frac{\omega_p}{\omega_s})(\frac{g_R}{A_{eff}})P_s P_P, \tag{2.34}$$

$$\frac{dP_s}{dz} = -\alpha_s P_s + \frac{g_R P_s P_s}{A_{eff}}, \tag{2.35}$$

where g_R is the Raman gain and α_s and α_p account for the fiber loss at Stokes and pump frequency, respectively. The Raman gain is the energy earned after the scattering and can be derived from the gain spectrum in Figure 2.9.

In order to derive the gain condition the Raman threshold must be computed, which is the input pump power at which the Stokes power is equal to the pump power at the fiber output. If the pump depletion is neglected ($P_s << P_P$), the pump power exponentially decays and the Stokes beam satisfies the following relation

$$\frac{dP_s}{dz} = \alpha_S P_s + \frac{g_R}{A_{eff}} P_0 e^{-\alpha_P z} P_S. \tag{2.36}$$

The solution for the above differential equation is

$$P_s(L) = P_s(0)exp(\frac{g_R P_P L_{eff}}{A_{eff}}). \tag{2.37}$$

Equation 2.37 is used to calculate the threshold. For instance, if the Raman gain spectrum shown in Figure 2.9 is approximated with a Lorentizian shape then the Raman threshold for a forward wave will be

$$P_{th} \approx 16\frac{A_{eff}}{g_R L_{eff}}, \tag{2.38}$$

where $A_{eff} \approx 50\mu m^2$, $g_R \approx 10^{-13} m/W$ and for $\alpha = 0.2dB/km$, $L_{eff} \approx 1/\alpha \approx 21.7km$.

The same analysis can be carried for a backward beam, the solution is almost equal to Equation 2.38 except for the factor 16 which is replaced by 20.

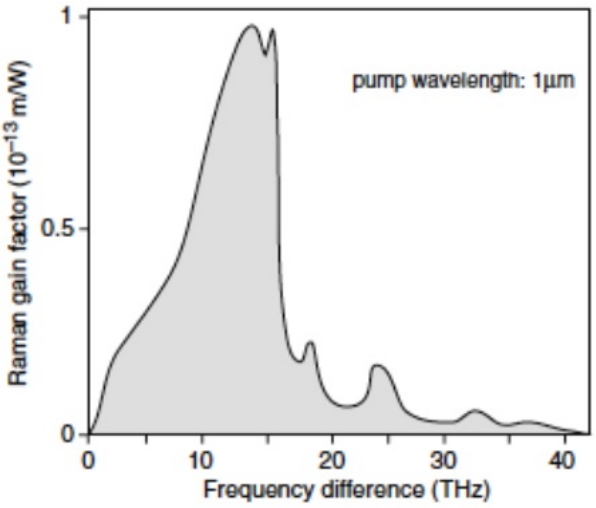

Figure 2.9: *Raman gain spectrum for fused silica [16].*

Finally notice that the process can be also studied as a special case of four wave mixing.

Stimulated Brillouin Scattering

The input power needed for stimulated Brillouin scattering is lower compared to SBS. Once the Brillouin threshold is reached, it manifests with the propagation of a backward Stokes waves carring most part of the input energy.

More in details, the pump induces a density variation in the material called electrostriction, which is seen as variation in the material refractive index. In fact, it can be described as a grating allowing the generation of Stokes wave through Bragg diffraction. The beat of both the pump frequency ω_p and the scattered light ω_s at the acoustic phonon ω_a enhances the acoustic wave resulting in coherent gain. Conversely to Raman scattering, the frequency shift depends on the scattered angle and can occur only in forward direction.

It is fundamental to compute the threshold power, defined as the incident power at which half of the pump power is transferred to the Stokes field at the output end at a fiber length L. As example, if the attenuation is $\alpha = 0.2dB/km$ and $L_{eff} \approx 21.7km$, the gain $g_B \approx 5 \cdot 10^{-11} m/W$ and effective area of $50\mu m^2$, then

$$P_{th} \approx 21 A_{eff}/(g_B L_{eff}) \approx 1mW. \tag{2.39}$$

The Brillouin gain, which follows the below equation, is frequency-dependent which is a consequence of the finite damping time T_B of acoustical waves

$$g_B(\Omega) = \frac{g_B(\Omega_B)}{1 + (\Omega - \Omega_B)^2 T_B^2}. \tag{2.40}$$

However, this scattering effect is usually considered detrimental because it removes power from the signal and it is further enhanced in single-channel systems. Additionally backward propagating Stokes waves disturb the transmitter in communication system. Nevertheless, the spectrum is narrow (reported in Figure 2.10) and can be used for narrow-bandwidth amplifier and laser design.

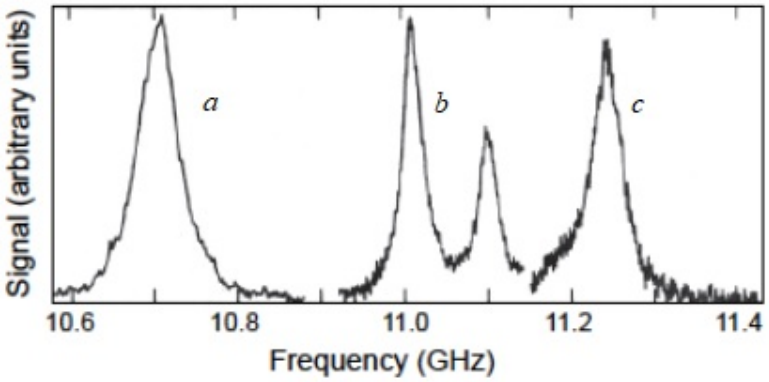

Figure 2.10: *Brillouin gain for a) dispersion-shifted fiber b) depressed-cladding fiber and c) silica-core fiber [17].*

In Table 2.2, the two processes are compared.

Table 2.2: *Comparison between SRS and SBS.*

SRS	**SBS**
Forward and backward directions	Backward direction
Almost 40 THz	Doping-dependent
Broad spectrum ($\approx 13THz$)	Narrow spectrum (Few MHz)
Low peak value	100 times higher

Chapter 3

Supercontinuum generation in microstructured optical fiber

Supercontinuum is a high-bright light source generated from the interplay between nonlinearities and dispersion effects. Its footprint is the ultra-broadened spectrum obtained by propagating an ultra-short pulse into a nonlinear medium. The current state-of-art is using optical fiber, in particular microstructured optical fiber thanks to its high nonlinearities.
In this chapter the basis of microstructure optical fiber are investigated first. Thus, the main parameters affecting the generation of SC and its fundamental generation mechanisms are studied, together with some examples taken from literature. Finally, the principle of fiber laser is briefly introduced and the experimental setup described.

3.1 Microstructured optical fibers

Light propagation into an optical fiber is typically described in terms of ray optics, which the phenomenon of exploits total internal reflection. However, this is true only if the variation of the refractive index is obtained by spatially varying the glass composition.
In the recent years, a new structure spreads over due to its versatility and freedom in the design which allows its use among different field of applications. These fibers, called *photonic crystal fibers*, have a holey cladding composed by an arrangement of densely close spaced air hole which extend through the entire fiber length and a solid-state core, as shown in Figure 3.1. Air holes reduce the refractive index of the glass increasing the contrast and leading to a stronger confinement in the core.

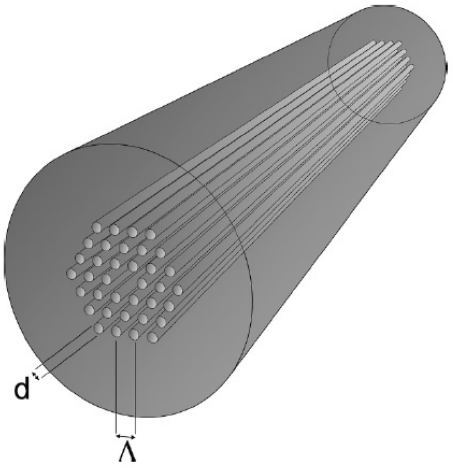

Figure 3.1: *Design of a microstructured optical fiber: circular holes form the cladding, while the core is made of a solid-state silica [18].*

The guiding properties are dependent on the two hole parameters, the diameter d and the hole-to-hole pitch Γ: their variation allows the control of air filling factor, defined as the ratio of the hole diameter to the hole-to-hole pitch. Thus, the possibility of tuning the effective refractive index of the cladding rises and is accomplished by the tailoring of the normalized frequency, defined as

$$V_{MOF} = \frac{2\pi a}{\lambda}\sqrt{n_{core}^2 - n_{clad}^2}, \tag{3.1}$$

where a is the core diameter.
Since the normalized frequency depends on the filling factor, for a particular value of Γ and d the condition of *endlessly single mode* [19] is reached. It means that no matter at what frequency the signal travels, there will be always just one mode propagating into the fiber. This behaviour could be justified as follow. The air holes acts as a modal sieve, accordingly when the fundamental mode is propagating into the fiber light cannot escape because silica gaps between the air holes encircling the core are too narrow and the mode does not fit in. For higher modes the lobe sizes are smaller and light is trapped between gaps, therefore by properly selecting d/Γ it is possible to guarantee the propagation of only the fundamental mode [20]. Figure 3.2 shows different characteristic curves at different FF: a low value of FF allows the fiber to operate in the single-mode regime.

Nevertheless, the application of these fibers for the supercontinuum generation is not widespread. In fact, the need of strong confinement and high nonlinearities require a high filling factor. Consequently, most MOF fibers used in the white light lasers [21] exhibit multi-mode behaviour. However, their excitation results

hard to obtain due to the high wavevector mismatch between the fundamental and higher-order modes.

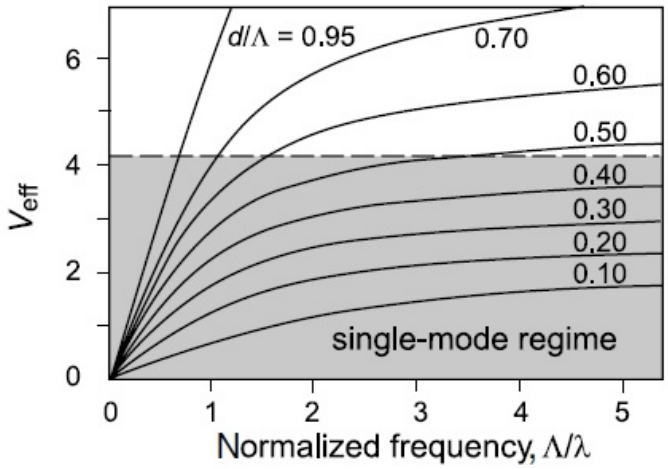

Figure 3.2: *Characteristic curve for different values of filling factor [18].*

Concerning the dispersion property of the fiber, the group velocity dispersion has the following mathematical expression

$$GVD \approx D_W + D_M = -\frac{\lambda}{c}\frac{d^2 n}{d\lambda^2} + D_M, \tag{3.2}$$

where D_W and D_M are the waveguide and material dispersion, respectively. For a particular value of wavelength, called zero-dispersion wavelength, the GVD is null meaning that two dispersions compensated each other. Especially in small-core photonic fibers, the ZDW has been observed in the visible region [22]. In light of this important discover, not only the single-mode regime can be tuned: nonlinearities and ZDW turn to be controllable variables. For these reasons MOFs are greatly used in a vary large range of application. Unfortunately, they are harder to manufacture and therefore quite expensive. They also have much higher loss than conventional fibers, and mechanically not nearly as robust [18]. Nevertheless, their properties are attractive for fiber lasers and amplifiers, telecom components, fiber-optic sensors of various kinds, quantum optics and, in the case of interest for this work, nonlinear device for supercontinuum generation.

3.2 Mechanisms behind SC generation

Supercontinuum generation is a process where laser light is converted to a very broad spectral bandwidth [23]. The process behind the generation of this ultra-large spectrum is selected from the combination between pump-pulse and fiber parameters. MOF is the material of choice thanks to its tailorable dispersion properties and strong nonlinearities induced by its structure. In Table 3.1 all parameters affecting the generation of the SC are listed. As stated, the dispersion is highly influenced by the wavelength and the unique advantages of photonic crystal fibers allow the fulfillment of experimental needs by modifying the core parameters (hole diameter and hole-to-hole pitch) and the fiber length. On the other hand, the properties of the input pulse are fundamental for the propagation of the pulse in the fiber and it must be chosen properly.

Table 3.1: *Parameters affecting the physics behind the SCG.*

Pump-power	**Fiber**
Width	Dispersion
Peak power	Core
Wavelength	Length

The temporal regime of the pump source has also a fundamental role in the creation of the supercontinuum. In fact, according to the temporal width different nonlinearities can take place. For this reason the main sources adopted in the different temporal scale are listed below.
The nonlinear mechanisms initializing the SC are summarized in the diagram sketched in Figure 3.3 taking into account all the possible combinations of dispersion and temporal regime.

- Nanosecond regime $\Delta\tau \approx ns$: Q-switched Nd:YAG laser ($\lambda = 1064nm$)
- Picosecond regime $\Delta\tau \approx ps$: Kr laser ($\lambda = 650nm$), Er^{+3} laser ($\lambda = 1550nm$)
- Subpicosecond regime $\Delta\tau \approx fs$: mode-locked Ti:Sapphire laser ($\lambda = 800nm$), Cr:F laser ($\lambda = 1250nm$)

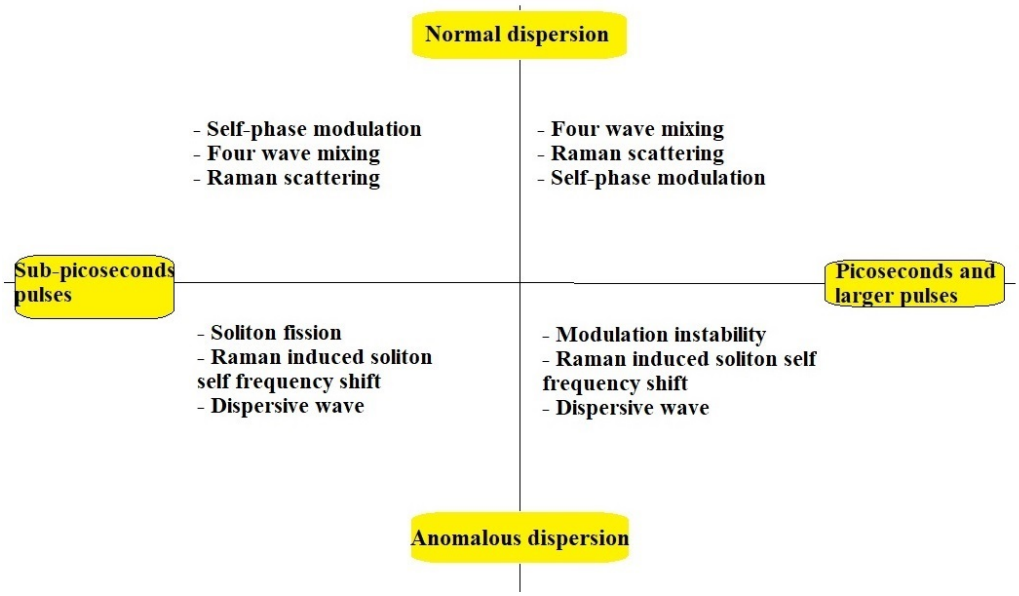

Figure 3.3: *Dominant mechanisms of SCG according to dispersion and temporal pulses.*

In the following different studies concerning SC are reported: firstly the supercontinuum generated in the nanosecond regime is proposed, then the pulse width is decreased to picosecond and sub-picosecond range.

Nanosecond regime

Many studies have been conducted in this temporal range and of particular interest is the work of *Dudley et al.* [24] which uses as source a Q-switched Nd:YAG laser emitting at 1064 nm. The study reports the excitation of both the fundamental mode LP_{01} and the first harmonic LP_{11}. The latter is supposed to be excited by the so-called multimode phase-matched parametric process, which is neglected in order to focus the attention only on the nonlinear and dispersive processes which involve LP_{01}. As shown in Figure 3.4, in normal dispersion condition the process begins with a Raman scattering, in fact Stokes and anti-Stokes peaks are clearly observable at 545 nm and 520 nm, respectively. The SC generation has been interpreted as a two-steps process [25]: firstly, the energy injected by the laser source is transferred in the surrounding of the ZDW in form of SRS effect, then FWM takes place. Conversely, in the anomalous region the process is conducted by solitons propagation.

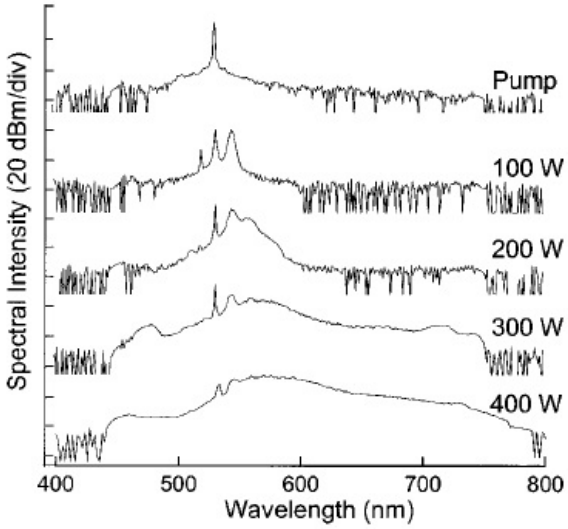

Figure 3.4: *Spectrum obtained by [24] for a light pulse in nanosecond regime under normal condition.*

Picosecond regime

As reported from the work of *Novotny et all.* [26], different mechanisms initialize the generation depending on the type of dispersion. The system developed can work in both VIS and IR regions, using a silica MOF with ZDW at $\lambda = 778nm$. In the infrared region the group velocity dispersion is negative leading to a positive dispersion and the SC is generated as a result of soliton dynamics. Instead, when considering the visible range the dispersion is positive and the system is under normal condition: an interaction between IR solitons and the visible pump leads to a blue-shift of the spectrum under the form of cascaded cross-phase modulation.

Femtosecond regime

Extensive researches have demonstrated that pulses with this temporal width have the broadest supercontinuum band. The pulse source commonly used is a mode-locked Ti:Sapphire laser with wavelength emission at 800 nm, alternatively a Cr:F laser at 1250 nm has been also used in some studies.
Supposing to be in the normal dispersion region the SC is initialized by the SPM, then the combination of FWM and Raman scattering further broadens the spectrum. In the study conducted in [26] this is clearly demonstrated. As shown from Figure 3.5, the broadening of the spectrum is symmetrical due to the SPM at low input power (a). Although, if this is increased the broadening starts becoming asymmetrical because of the Raman shift and new frequencies are generated in

the red region of the spectrum (b-c). At even higher power the self-steeping effect appears, clearly observable from the emerging tail in the blue-range (d). Notice that solitons cannot propagate in normal dispersion and no supercontinuum is created above the ZDW.
The largest spectrum is obtained only when the pump frequency lies in the vicinity of the ZDW. In the case reported ZDW is at 950 nm, although the spectrum in the above figure has been sensed for 746 nm which is far away from the ZDW. Nevertheless, if the pumping wavelength is pushed closer to ZDW the spectrum would be broader: in fact, it enlarges towards red frequency given enough energy for FWM effects.

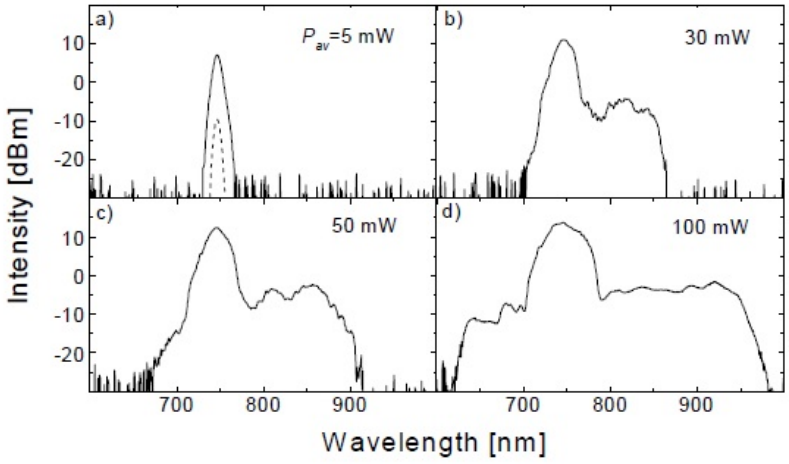

Figure 3.5: *Pulse evolution for $\lambda_{pump} = 746nm$ in normal dispersion condition [26].*

In the anomalous region different mechanisms are in play. In Figure 3.6, the spectrum evolution for pumping wavelength at 804 nm is reported. The initial symmetrical pulse is simultaneously jagged in both red-shifted Stokes sub-pulses and blue-shifted anti-Stokes components near the ZDW. As the input power increases, more peaks appear and the width of SC is broader and more asymmetrical. The jaggedness of the pulse is due to the compression caused by the combination of nonlinearities and anomalous dispersion. When the equilibrium between the two mechanisms is reached, solitons are generated. Therefore, Raman scattering causes a shift of solitons beacause of a perturbation induced by the high-order dispersive terms. Consequently, to maintain their shape unaltered they irradiate energy under the form of anti-Stokes peaks. On the other side, in the blue range the creation of dispersive waves is observed.

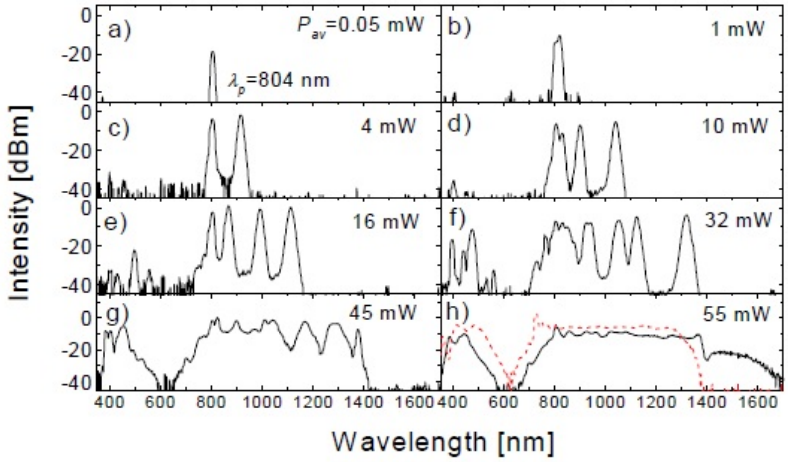

Figure 3.6: *Temporal evolution of input pulse in anomalous dispersion region [26].*

After the comparison of different cases, the main consequences of the time scale variation can be summerized. In femtosecond regime, the SC is generated within the first centimeter of MOF whereas in nanosecond range the fiber has to be longer. Additionally, in the first case the spectrum is well-wide and good properties are obtained. Nevertheless, the device is quite cumbersome and for this reason larger pulse width are preferable since the device can be more compact.

Chapter 4

Picosecond supercontinuum light source

In this work, the generation of the supercontinuum is performed as a combination of a gain-switched fiber laser and a two-stages amplifier.
The main concepts for the understanding of the experimental setup are described in this section. Firstly, the working principle of gain-switching and Q-switching are presented together with drawbacks and benefits. In particular the reasons behind the choice of GS are highlighted. Successively, a brief presentation of the fiber laser design is presented. Finally, the experimental setup is described.

4.1 Gain-switched laser as pump laser

Both gain-switching and Q-switching are techniques used to generate a high-repetition-rate pulse train. Even though their working principle is similar and can be described by the same numerical model [27], GS presents interesting properties which lead to a deeper investigation in different field of applications in the recent years.

Q-switching

The modulation of both cavity losses and quality factor is exploited to create an energetic pulse train at nanoseconds repetition for solid-state lasers. A typical experimental setup is illustrated in Figure 4.1 which is composed by: a high reflective concave mirror, an output coupler which transmit first or higher order modes, a laser gain medium and a modulator (which can be either electro-absorption or electro-optics). When the laser is turn on and the modulator is switched off, the light is reflected back from the mirror and transmits an almost perfect Gaussian

profile at the output. If the modulator is on, the resonator losses are kept at a high level in order to avoid the lasing condition and, at the same time, feed the gain medium with pumping energy. Suddenly, the losses are reduced to a small value allowing the quick build up in the resonator. The control of losses, which can be done either passively or actively, leads to the pulse peak once the lasing conditions are satisfied. The alternating repetition of high and low cavity losses generates high repetition pulses in the nanosecond regime, as shown in the diagram in Figure 4.2.

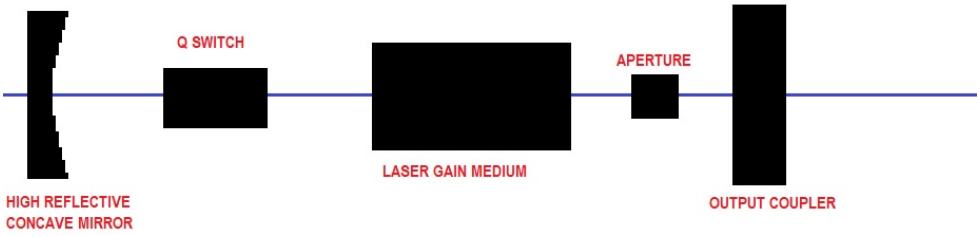

Figure 4.1: *Schematic setup of a Q-switched laser.*

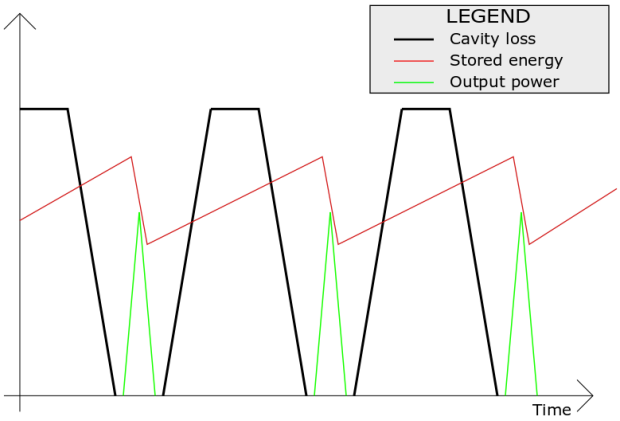

Figure 4.2: *Temporal evolution of stored energy, cavity losses and output power in a Q-switched laser [28].*

Gain-switching

Contrarily to Q-switching, gain-switching is based on the modulation of the gain. Generally, this method is applied to rare-earth doped material for their high gain coefficient and it is usually used in fiber laser. The setup is outlined in Figure 4.3: the light emitted from a pulsed pump source travels into a fiber and passes through an isolator, placed to avoid the damage of the source. Then, it is guided through a cavity made of a doped fiber surrounded by two fiber Bragg grating, the first one works as high reflection coating and the other as anti reflection coating. Finally, the pulsed wave outputs. An alternative configuration is the ring structure.

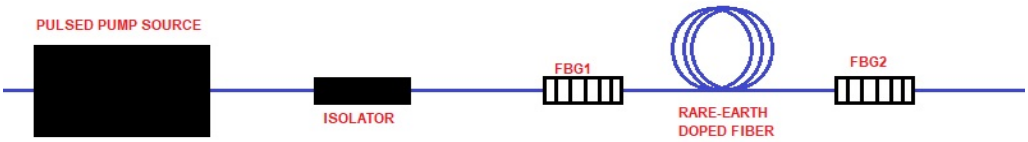

Figure 4.3: *Schematic setup of a gain-switched laser.*

The main differences between the two techniques are well-explained by *Jung et al.* [27].
Figure 4.4 reports the physical process of both Q and gain switching in terms of intensity and population temporal evolution. The pump interval pointed out in the plot is referred to the width of the pump pulse in gain-switching, while in the case of QS it is the duration of CW pump before the cavity losses are switched. Before reaching the lasing condition the two switching methods coincide, although when the threshold is archived different behaviours are observed. GS start lasing with a slightly increase of the population and it stops accumulating when the pump pulse ends. On the contrary, at the beginning of the lasing QS continues to accumulate carriers with a larger rate and it is arrested at the switching of cavity loss. Despite the differences, in both systems the upper level population is consumed rapidly and the lasers keep growing. Finally, when the system goes back to the threshold condition the peak is reached. As it is observed, below the threshold emission continues due to the higher rate of the spontaneous emission compared to the one of the stimulated emission. Moreover, if the peak of the QS is high and narrow for GS it has a lower value and broader shape.

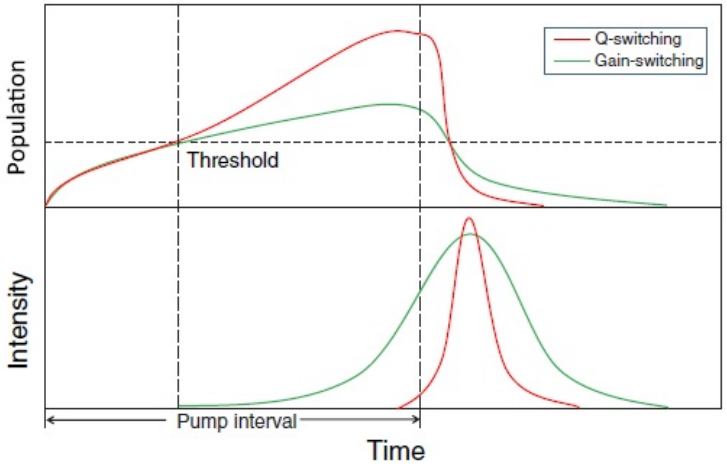

Figure 4.4: *Temporal evolution of population upper state and intensity for Q-switching and gain-switching [27].*

Both GS and QS are able to generate nanosecond pulse train, although some advantages makes GS the method of choice. Firstly, it is possible to implement an all-fiber configuration which increases the compactness of the device. Furthermore it has a very simple geometry capable to transmit single mode and high pulse energy. Last but not least the spectral coverage is very wide and the use of FBG allows very narrow bandwidth of the order of nanometer.

4.2 Fiber laser

In this study, the generation of the supercontinuum is based on the use of a fiber laser. Recently, the evolution of this architecture has been grown fast due to the its several advantages. In fact, the pursuit of higher output power together with the need of high brightness pushed researchers to overcome the shortcoming of the conventional solid-state lasers. Indeed, even if they have the best performance in terms of both output power and brightness, the quantum defects sets a limit in their efficiency [29]. In other words the energy gap between the pump and the lasing condition, which is the quantum defects [30], heats the gain material inducing a thermal stress. This leads to birefringence and, consequently, a worse quality beam. If a good quality beam has to be maintained, a power scaling is necessary which is affected by thermo-optics issues.

Fiber lasers not only overcome solid state laser limitation, they have outstanding performance in terms of output power, beam quality, overall efficiency, and flexibility concerning operating wavelength and radiation format [31]. These good qualities derive from the all-fiber design.

As sketched in Figure 4.5, the light from a pump laser diode is launched into a rare-earth doped fiber which constitutes the active core. Subsequently, in order to reach the lasing condition the light resonates in a cavity. Once the threshold is reached the laser outputs from the fiber which is guided in the same waveguide of the pump laser.

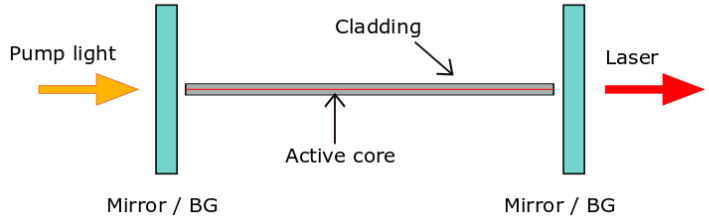

Figure 4.5: *Schematic illustration of fiber laser with a linear cavity resonator.*

The co-propagation of the laser and pump light in the same waveguide allows compactness and long-term stability of the structure, since there is no need of free-space components. Another consequence is the maintenance of the light intensity along the fiber which makes the structure free from diffraction limitations. Furthermore, if a single mode core is adopted the laser is able to emit an almost perfect Gaussian beam which gives a high quality beam.
Since the gain medium is made long and thin, the surface-to-volume ratio is high and enables an easy thermal dissipation to the surroundings [32]. Moreover, the long length provides huge single-pass gain which opens further study for power scaling [33].
Further profits are high gain and low threshold power. Firstly, the gain of the laser is given by the product of pump intensity and the interaction length between radiation and gain material. Several tens of meters long fiber are allowed thanks to the low losses of the rare-earth dopants. Hence, these increase the gain which leads to high efficient operation systems from relatively low-brightness diode pump radiation to high-brightness laser output.
Due to the many parameters in play the structure of these lasers is tailored in order to improve the performances and satisfy the power needs. For this reason

they can be classified according to the cavity design, pumping scheme, dopants and operation regime. However, fiber lasers present challenging restrictions as the decrease of the peak power caused by nonlinearities, photo-darkening, degradation and dispersion which affects mainly short-pulses.

Laser cavity design

Two cavity designs are available: a linear configuration and a ring shape. Figure 4.5 shows the simplest architecture of a fiber laser: the light from a pump source is launched inside an active fiber and it resonates due to a Fabry-Perot cavity. This is realized with a couple of mirrors or, alternatively, two Bragg gratings. Nevertheless, this configuration makes the pumping difficult because of the small volume of the fiber [34]. For this reason the efficiency can be increased by butt-coupling highly reflecting dielectric mirrors to the fiber facets. Other options include the creation of fiber Bragg gratings (FBG) at fiber ends or using passive fiber components as Sagnac loops.
Conversely, ring-fiber lasers have a cavity formed by a passive loop fiber and couplers to provide uni-directional feedback. The ring configurations have been tailored in order to lower the pump power threshold in the linear cavities. Although, a compromise between threshold power and efficiency must be reached since the ring configuration has the lowest threshold, whereas the linear cavity excels for both high output power and efficiency [35]. All structures are shown in Figure 4.6.

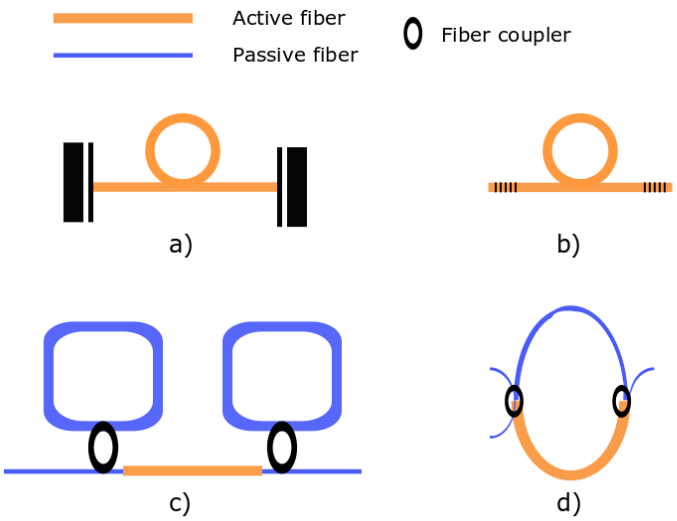

Figure 4.6: *a) Fabry-Perot cavity with dielectric mirrors, b) FP cavity with Bragg gratings, c) Sagnac loop and d) ring cavity.*

Pumping scheme

The pump laser can be either a diode or a fiber laser and have different active fiber design according to the required output power. Generally, the pumping can be classified as core and cladding pumping. When output power of few watts are needed the core-pumping configuration is the choice, on the contrary for high power application the cladding-pump is used. The core-pumping system has been proposed in the paragraph above, whereas the cladding-pump has different fiber design. Indeed, an additional cladding layer is added to create a secondary waveguide which is highly multi-mode [36]. This inner cladding can guide light launched from low brightness high-power diode laser. During the propagation light is absorbed and converted into high brightness and power laser. This is caused by the higher NA and larger core area which allows both the collection of more light and the reduction of the pump beam quality. However, an efficiency degradation can occur since in the inner cladding the intensity distribution do not overlap with the doped core as in the core-pumping. Consequently, there is lower absorption compared to the other configuration. This is clearly shown in the plot in Figure 4.7 (b).

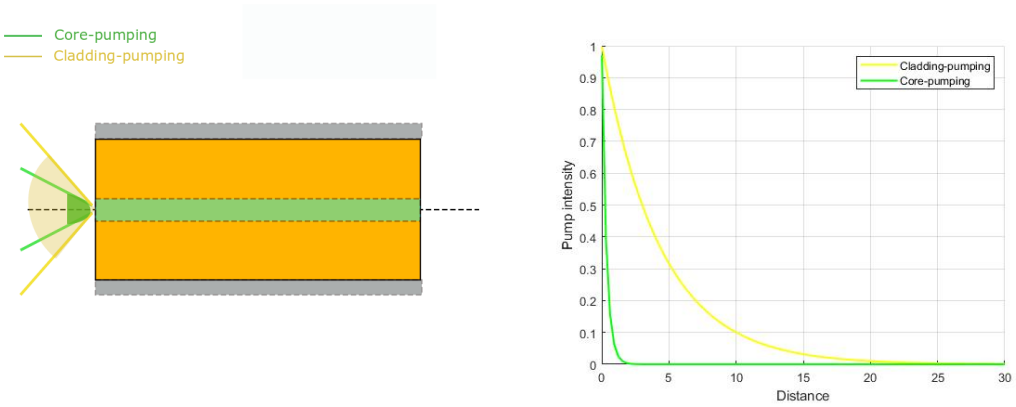

(a) **(b)**

Figure 4.7: *a) Schematic configuration of cladding and core pumping b) pump intensity as a function of fiber length.*

Rare-earth dopants

The active material is made of a glass fiber doped with rare-earth elements. Their insertion in the material matrix increases the Rayleigh scattering which is considered the main drawback of this doping, nevertheless the advantages are multiple and cannot be compared to the loss increase caused by the higher scattering rate.

Erbium and ytterbium are the most important elements since they can be

adopted in a huge variety of field, for instance in telecommunication and high power lasers [37]-[38]. In the case reported in this thesis, the element of choice is Ytterbium for different reasons. Firstly, it has the lowest value of quantum defect (10 < %) which increases the efficiency. Secondly, the gain is high and leads to a high output power. Despite all, the advantages of Ytterbium come from its electronic structure which is a two-levels structure. This balances the constrains introduced by the dopants in the host material and avoids both excited state absorption and non-radiative decay.

4.3 Experimental setup

The experimental setup of this work is presented in Figure 4.8: the light emitted from a gain-switched laser diode is amplified in a two-stage fiber amplifier and successively the supercontinuum is generated after the optical pulses have been launched into the microstructured optical fiber[1].

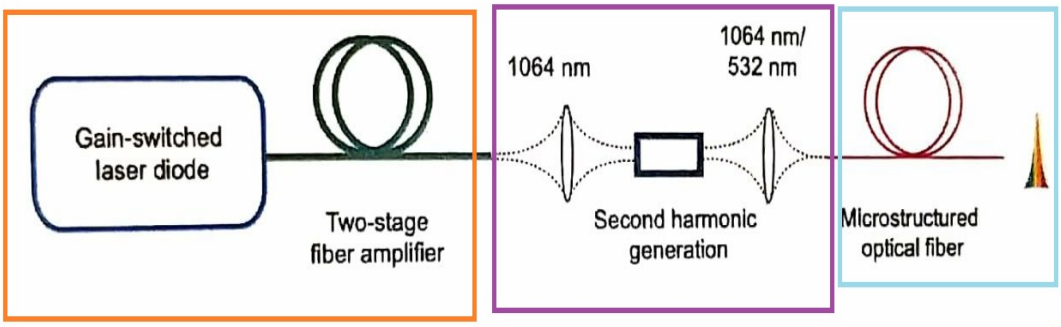

Figure 4.8: *Basic scheme of the picosecond supercontinuum light source.*

More in details, after the emitted pulse from a GS laser diode has been amplified, a part of its output is frequency-doubled leading to the creation of two pulses at the frequencies of 532 nm and 1064 nm, which are launched inside a MOF to generate a supercontinuum by means of a dual-wavelength pumping scheme. The latter is been adopted since lower coupling power is required compared to single-wavelength pumping when generating SC in the visible range. The setup can be divided in three main areas, deeper analyzed in the following.

[1]The light source described has been proposed and studied by *S. Novotny et al., "Picosecond supercontinuum light source for stroboscopic white-light interferometry with freely adjustable pulse repetition rate," Opt. Express 22, 13625 (2014).*

1. Gain-switched laser diode and two-stage fiber amplifier

The amplification of the generated pulse is able to provide a sufficient pump power for the SC thanks to kW peak power. Moreover, it guarantees an unique frequency choice flexibility among a wide range.

The characteristic of both the laser diode and two-stage Yb amplifier are listed in Table 4.1.

Table 4.1: *Specification of picosecond pump laser source.*

Gain-switched laser diode	**Two-stage fiber amplifier**
Picopower-LD-1064-FC-SF-50 (Alphalas Gmbh) Wavelength $\lambda = 1064nm$ Repetition rate: 0 - 50 MHz Pulse width: $\approx 50ps$ at 1MHz	Ytterbium-doped polarization-maintaining fibers (LiekkiTM) Stage 1: 1 m long Yb700-6/125-PM] Stage 2: 2.5 m long Yb1200-12/125DC-PM

The amplification scheme is proposed in Figure 4.9. Light generated by the GS laser diode propagates through a polarization maintaining fiber, an optical isolator (OI) and a bandpass filter (BPF). These components prevent backward propagation of light and decrease the amount of amplified spontaneous emission (ASE). Subsequently, a single mode (SM) polarization-maintained pump laser emitting at 974.5 nm core-pumps in forward direction the active fiber of the first stage amplifier. After the amplification, the pulse travels through the optical isolator, the band-pass filter and the cladding power stripper till it reaches the second stage amplification. Differently from above, the signal is cladding-pumped in backward direction by a 976 nm multi-mode MM-pump. The system GS laser and PM fiber are synchronized with an external trigger since a tuning of the repetition rate up to 50 MHz is required.

In order to guarantee a strong and efficient coupling among the stages the fiber must be properly spliced. In fact, due to its polarization maintaining nature it is necessary to carefully cleave and align the fiber facets in order to avoid high loss. A thermal PM splicing is the suitable process since the two fiber ends are heated and softened at $\approx$ 2,000° through the application of an electric arc. An extremely control of both core alignment and cleaved facet determines the loss of the splicing and consequently determines its quality.
Different alignment methods are available: core, cladding and active alignments. The former is based on the use of a PM splicer with Yb fibers, which enables the operator to manually align the core octagonal sections of the two fiber ends. At the end of the operation a loss testing is required to assess the goodness of the splicing. If the core alignment is considered one of the highly performing methods, the cladding alignment is not recommended for optimal results.

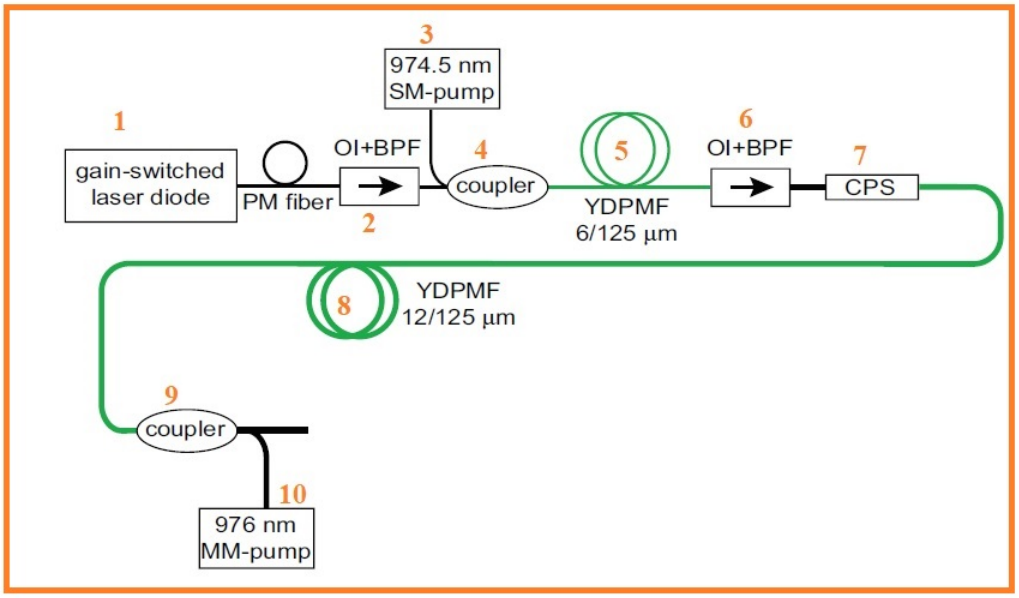

Figure 4.9: *GS laser diode and two stage amplification: 1) GS laser diode, 2) OI+BPF, 3) SM-pump, 4) coupler 5) YDPMF, 6) OI+BPF, 7) CPS, 8) YDPMF, 9) coupler and 10) MM-pump.*

Finally, the best solution is to apply an active alignment. The transmission of a probe signal, generally a LED light source emitting at 1200 nm, is measured. The technique is based on three steps: firstly the initial power of only the core is measured by means of a powermeter. Then, the optimization of the signal transmission takes place by aligning the two facets. Once the optimal position is reached the two fibers can be joined together. A fundamental aspect of this method is the stripping of the cladding light before the powermeter, if it is not done properly it can badly affect the loss splicing measurement.
In this thesis, the core alignment has been applied for every spliced points. Subsequently, it must be protected through a fiber recoating. It consists in curing a high index acrylate polymer under UV light by making use of proper tools.

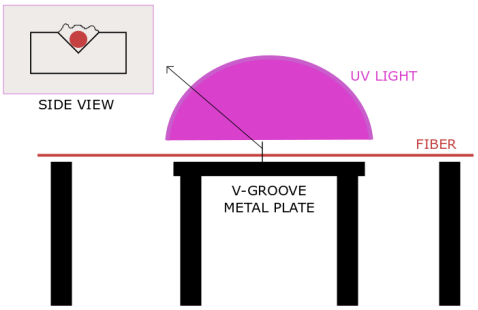

Figure 4.10: *Schematic setup for recoating process.*

Unfortunately, due to the unavailability of the recoater a manual recoating process was chosen. The setup is proposed in Figure 4.10: the spliced fiber lays on a V-groove metal plate and is tightened by two lateral fiber support. The uncover part of the fiber is immersed in the polymeric resin and the V-groove plate acts as a mold. The fiber is hold on in position under the UV light source and then the curing process begins.
The typical coating thickness is $125\mu m$ which is not reachable with this setup, nevertheless a fair result has been obtained.

2. Second harmonic generation using free-space optics

The frequency-doubling is realized through the generation of the second harmonic. After the amplified light has been collimated using an optical isolator and a band pass filter, it passes through a 5 mm long Potassium Titanyl Phosphate (KTP) with a maximum conversion efficiency of $\approx 22\%$. Further details on the frequency-doubling crystal are given in Appendix 5.1.2. The setup, shown in Figure 4.11, consists of the following components:

- Collimating lense L1;
- Band pass filter and optical isolator;
- Lambda/2 wave plate;
- Focusing lense L2;
- KTP crystal;
- Collimating lense L3;
- Microscope objective;

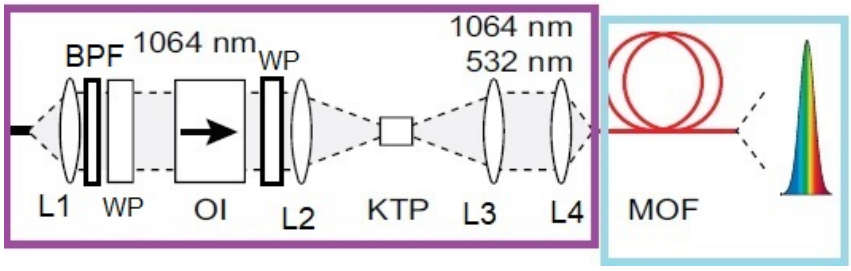

Figure 4.11: *Diagram of second harmonics generation and MOF: a portion of the amplified pulse is frequency-double thanks to KTP crystal, then two pulses at 532 nm and 1064 nm are collimated in MOF to generate the supercontinuum .*

Once the optical components are all mounted, a proper alignment of the setup must be performed. Additionally, in order to reach the highest conversion efficiency of the KTP its optimal position has been found by combining both tilt and rotational angle displacement together with power measurements, as better described in Chapter 5.

3. Microstructured optical fiber

After the proposed MOF (Figure 4.12) couples the two signals at 532 and 1064 nm, a dual-wavelength pumped supercontinuum is generated. Nevertheless, the input efficiency is strongly affected by the chromatic aberration which turns to be $\approx 9\%$ and $\approx 17.5\%$ for 592 and 1064 nm, respectively.
Since light propagation in the fiber is dominated by both dispersion and attenuation, before any measurements the dispersion characteristic and the field modes propagating along the fiber must be known. For this purpose, the software *COMSOL Multiphysics*© [39] was used.

When dealing with the propagation of a signal into a fiber the wave equation must be solved

$$\nabla \times \frac{1}{\epsilon(\vec{r},\omega)} \nabla \times \vec{H}(\vec{r},\omega) = k_0^2 \vec{H}(\vec{r},t). \tag{4.1}$$

In the particular case of microstructure fiber, the ansatz introduced in the equation is

$$\vec{H}(x,y,z,t) = \vec{H}(x,y)e^{-i(\beta z - \omega t)}, \tag{4.2}$$

where $\vec{H}(x,y,z,t)$ it the magnetic field, $\epsilon(\vec{r},\omega)$ the relative dielectric function, k_0 describes the wave number at the free-space wavelength λ, ω is the frequency and t and $\vec{r} \equiv (x,y,z)$ denote time and space, respectively.

The Sellmeir equation is used to analyze the material dispersion

$$\epsilon(\lambda) = 1 + \sum_{j=1}^{M} \frac{B_j \lambda^2}{\lambda^2 - \lambda_j^2}, \tag{4.3}$$

both λ_j and B_j are tabulated values (for undoped silica their values can be found in [40]). In fact, the dispersion is defined as

$$D(\lambda) = -\frac{2\pi c}{\lambda^2}\beta_2 = -\frac{\lambda}{c}\frac{d^2 n_{eff}}{d\lambda^2}. \tag{4.4}$$

The parameter n_{eff} is defined as follows

$$n_{eff} = n(\omega) = \sqrt{\epsilon(\lambda)}. \tag{4.5}$$

The coefficient β_2 derives from the Taylor expansion of the mode propagation constant β

$$\beta(\omega) = n(\omega)\frac{\omega}{c} = \beta_0 + \beta_1(\omega - \omega_0) + \beta_2(\omega - \omega_0) + ... \tag{4.6}$$

The first derivative β_1 is correlated to the group velocity according to

$$\beta_1 = \frac{d\beta}{d\omega} = \frac{1}{v_g} = \frac{1}{c}(n + \omega\frac{dn}{d\omega}), \tag{4.7}$$

instead the second derivative β_2 is linked to the dispersion

$$\beta_2 = \frac{d^2\beta}{d\omega^2} = \frac{1}{c}(2\frac{dn}{d\omega} + \omega\frac{d^2 n}{d\omega^2}). \tag{4.8}$$

The differential equations are solved through FEM analysis: the wave equation is solved for a large set of properly chosen elementary subspaces [41]. If the continuity of the field is guaranteed, the geometry can be parcelled. Thus, a mesh of finite elements is created being composed by triangles and quadrilaterals in 2D case. Subsequently, Maxwell equations are applied to each element and result in a set of elementary matrices. The combination of these elementary matrices leads to a global matrix system for the structure analyzed. Finally, the effective index and the distribution of both amplitudes and mode polarizations are computed numerically applying the condition of continuity at each boundary.
In this work a *MATLAB* © [42] script has been used in order to design both the geometry and the mesh. In this way the control of parameters during *COMSOL* simulation results more affordable. The same script computes the dispersion characteristic by finding n_{eff} for each node of the mesh for a given frequency range. Thus, the first and second derivative are calculated in order to obtain the dispersion.

Table 4.2: *Parameters for the MOF having a triangular structure.*

Dimension	Parameter	Value [μm]
Hole pitch	Γ	1.55
Hole diameter	d	1.085
Core diameter	d_{core}	1.75
Fiber length	l	$7 \cdot 10^6$

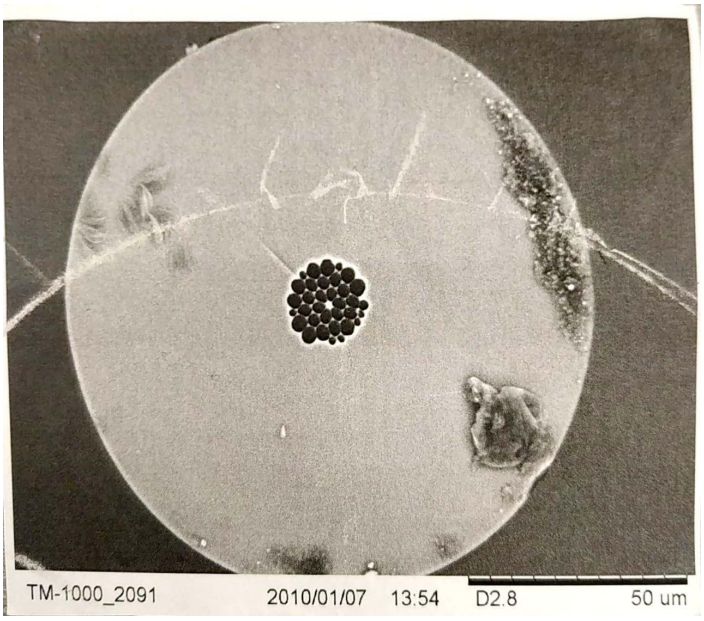

Figure 4.12: *SEM image of Uranus-1.*

Geometry and boundary conditions

The first step is to define the geometry. Figure 4.13 shows the fiber section and Table 4.2 lists its dimensions. The simulations have been run using a quarter of the fiber section. In this way it was possible to cut computational time by exploiting the fiber symmetry.
An external additional layer, called perfectly matched layer, has been inserted which behaves as an artificial absorbing layer for wave equations. It is commonly used to truncate computational regions in numerical methods to simulate problems with open boundaries and to avoid reflections [43]. Its thickness has been chosen such that $S_{PML} > \lambda/2$.

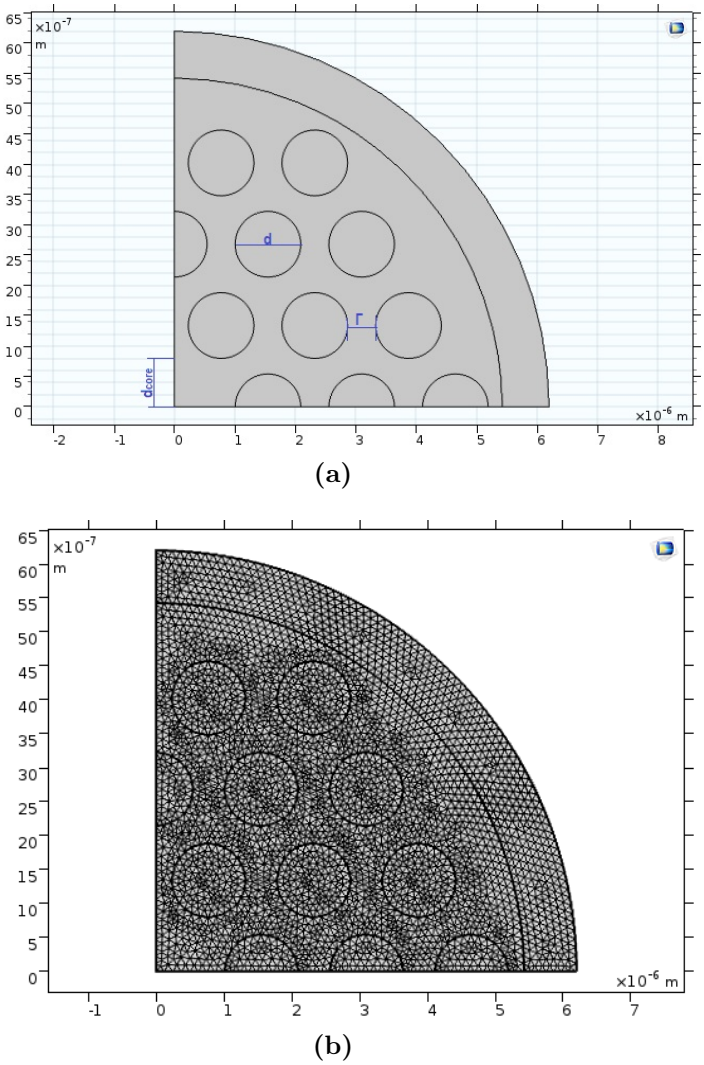

Figure 4.13: *MOF geometry and mesh in COMSOL Multiphysics environment.*

Mesh

The dimension of the domains has different size: it is extra fine in the core, while in both the cladding and PML has normal dimension. This has been set in order to cut computational time and have a better visualization of the solution in the area of interest, which is the core. Additionally, the mesh size criterion is given by $h_{min} > \lambda/5$ and the final result is presented in Figure 4.13 (b).

Simulations and results

Figure 4.15 shows the dispersion curve calculated in the wavelength range from 400 to 2000 nm. The fiber has been tailored in order to possess two zero dispersion wavelength, one at 780 nm and the other at 1900 nm. Furthermore, the simulation results showing both the electric field and intensity distribution for the fundamental mode are reported in Figure 4.14. Among the different solutions proposed from the simulation, the fundamental mode is the one with the highest value of effective refractive index. This parameter is defined also as

$$n_{eff} = \frac{c}{v_p} = \frac{\beta}{k}, \tag{4.9}$$

where c is the light speed, v_p defines the waveguide velocity. Consequently, it is the ratio of the free-space velocity to the material velocity. It depends on both the material properties and wavelength, hence it can be designed to be close to the cut-off frequency. In this case, the highest effective index is 1.337.
Simulations show a good light confinement within the core. In fact, only a small portion of the power is dispersed, as shown in Figure 4.14 (b).

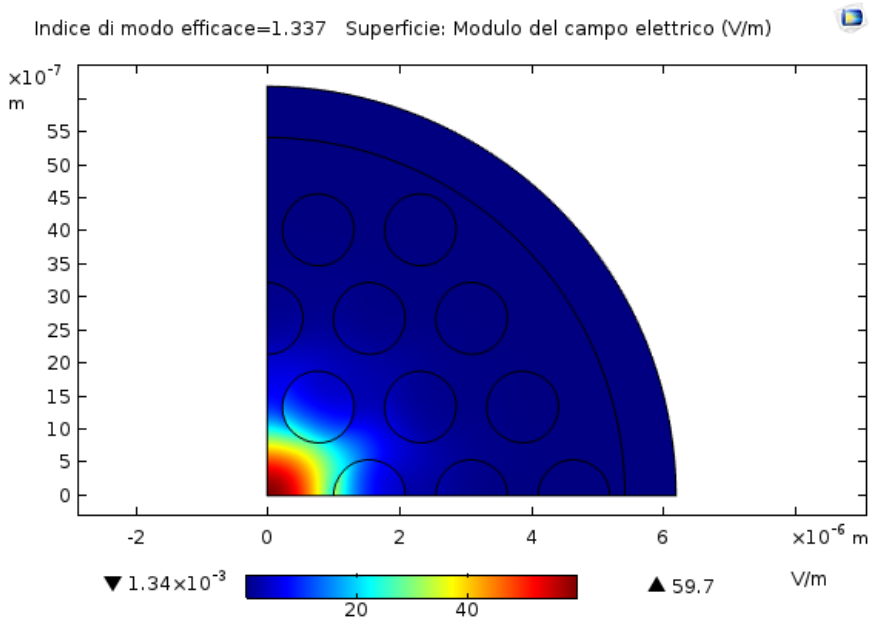

(a)

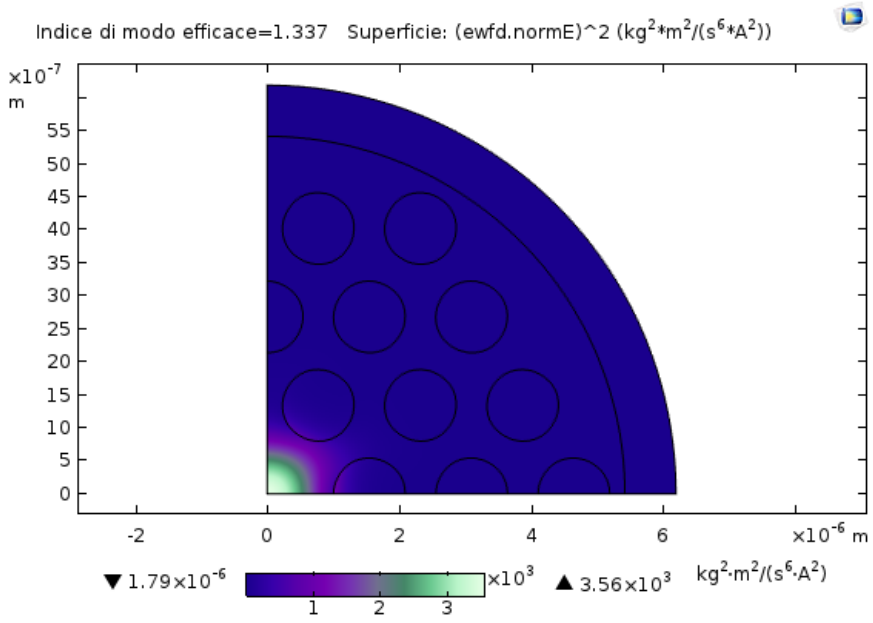

(b)

Figure 4.14: *a) Electric field distribution and b) power distribution of the fundamental mode for* $n_{eff} = 1.337$.

The fiber has been tailored in order to have two ZDW, as shown in the dispersion plot in Figure 4.15. In particular, the first ZDW is set at 778 nm which is in between the two pump wavelenghts. The inverse of the group velocity β_1 and the group velocity dispersion β_2 at 532 nm are $4.985 \cdot 10^{-9} s/m$ and $-5.079 \cdot 10^{-26} s^2/m$, respectively. Whereas, for 1064 nm $\beta_1 = 4.971 \cdot 10^{-9} s/m$ and $\beta_2 = -5.652 \cdot 10^{-26} s^2/m$.

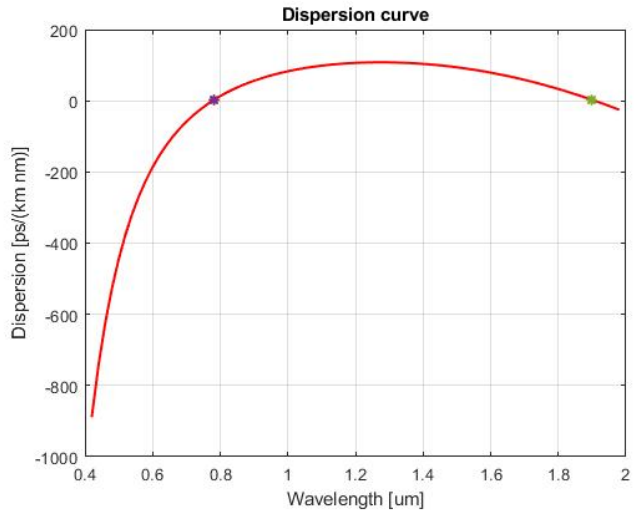

Figure 4.15: *Dispersion curve: the two ZDWs are set approximately at 800 nm and 1900 nm, respectively.*

Light-to-fiber coupling It is considered one of the most important and crucial step in hydrid optics [44] and a precise coupling between light and fiber guarantees the successful performance of the overall setup. Generally, there are three possible combinations of coupling: alignment, focusing and collimation. An efficient alignment of the optical components assess the minimum loss inside the system, while a good focusing and collimation strongly depends on the choice of the optical lens. Figure 4.16 shows the operating principle of a fiber collimator, notice that the focusing works in reverse.

G. Best and O.M. Sezerman [44] suggest an useful rule-of-thumb: in order to obtain 0.99 transmission through the optics, its numerical aperture must be at least 50% greater than the NA of the fiber. The following formula have been used to select the proper microscope objective for the launching of the light into the MOF.

$$BD[mm] = 2 \cdot f[mm] \cdot NA \tag{4.10}$$

$$DA[mrad] = \frac{a[\mu m]}{f[mm]} \tag{4.11}$$

where BD and DA are the collimated beam characteristics sketched in Figure 4.16, f is the focal length of the lens and NA is the numerical aperture of the fiber. The latter is equal to the root square of the difference between the square of core and cladding refractive index for multi-mode fiber, while for single-mode fiber this last definition leads to error. For this reason Gaussian optics is used and NA is given by $\frac{2\lambda}{\pi a}$.

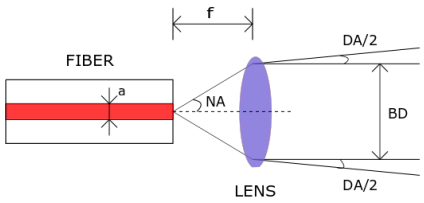

Figure 4.16: *Fiber collimator.*

Chapter 5

Results

The characterization of the fiber light source is essential before generating a supercontinuum. In fact, white light lasers depend not only on the fiber dispersion: pulse duration and peak power strongly influence its performance. In the previous chapter the dispersive properties were numerically calculated. In the following, the performance of the source is assessed in terms of output power, temporal pulse width, quality factor and spectral measurements. Successively, the spectral stability of the supercontinuum generated by coupling the light source into the microstructure optical fiber is checked.

5.1 Fiber laser performance

Modelling and simulations of the light source

To evaluate the goodness of the experimental data, a modelling of the setup was performed. Due to the spreading of fiber devices a lot of software tools are commercially available which help the designer to have a clear and transparent understanding of the device, avoiding waste of time and money.

In this work, *RP-Fiber Power* [45] was used to simulate the light propagation in the two-stage amplifier. The software allows modelling of both active and passive fiber whose characteristics are located in a large library of specifications and spectroscopic data. Furthermore, optical channels, as pump and signal inputs and even ASE, are easily simulated with huge flexibility. It is possible to arbitrarily select input powers, wavelength, radial function for intensity profile, losses, reflectivities, doping profile and propagation direction, which enable the prediction of the device performance, its optimization and the impact of eventual detrimental effects.

In this thesis, the two-stages amplifier was modelled based on the average powers which would have been converted in pulse properties afterwards. In principle, the analysis must be performed one stage per time in order to take care as much as

possible of every details, such as ASE and nonlinear effects. To demonstrate this statement two slots of simulations have been carried on: firstly the two stages of amplification have been modelled separately, then together. The latter is justified from the easier calculations since eventual nonlinear effects in the active fiber are deleted.
Both models work on a L-long active fiber set along the z coordinate, having assumed a constant doping concentration towards this direction. The fiber is sub-divided in N_z steps defined by the user, then the program computes the output powers and electron population for each step. The choice of the number of steps is critical for the coherence of the model, consequently it has been selected considering almost a gain of 30 dB for each segment. Once the parcelling of the model has been set, the software solves both rate and propagation equation considering the entire Stark level manifolds and using a wavelength-dependent effective transition cross section which allows the approximation of transitions between all sub-levels through a weighted average.

Hereafter the analysis of the separated stages are reported first, then it is followed by the two-stages simulation. In both cases, the characteristics of both the signal and pump channels are computed and then used as input parameter for the simulations.

First stage The Gaussian-shaped signal is generated from the GS laser diode at 1064 nm. The mode field radius of the signal is computed from the definition of divergence θ. In fact, the latter is known from the technical data-sheet and consequently the radius of the Gaussian beam ω_0 is computed from

$$\omega_0 = \frac{\lambda}{n\pi\theta}, \tag{5.1}$$

which results in 4.52 μm. Then the signal is launched into the amplifier: for instance, at 1 MHz it has an average output power of $20\mu W$ which corresponds to a peak power of almost 400 mW.

The active fiber *LIEKKI Yb700-20/125DC* is pumped at the maximum seed power which corresponds to an input current of 320 mA. As mentioned above, the first stage is core-pumping in forward direction at 974.5 nm which is supposed to behave as a LP01 mode. The pump power was set to 140 mW which is the average power of a Gaussian pulse at 1 MHz. The mode field diameter is estimated from the Petermann II formula [46]

$$\frac{w}{a} \approx 0.65 + \frac{1.619}{V^{3/2}} + \frac{2.879}{V^6} - (0.016 + 1.561 \cdot V^{-7}) \tag{5.2}$$

where a is the core diameter and V is the normalized frequency. The MFD results is 6.44 μm. It is important to mention that the NA has been calculated according

to

$$NA = \frac{2 \cdot \lambda}{\pi a}. \tag{5.3}$$

The numerical aperture could also be computed from the core and cladding refractive index, however it can cause significant errors [44].

The simulation results reported below considered an input Gaussian pulse at 1 MHz. The trend of the output signal power as a function of the fiber length is shown in Figure 5.1 (a). As it can be observed, after 70 cm the signal reaches the value of approximately 1.70 mW which is maintained almost steadily. The gain reached under these conditions is 19.4 dB which can be considered reasonable. In fact, if compared to the experimental results obtained by *S. Novotny et al.* [1] under the same conditions the authors obtained a gain of 15 dB.

Under saturation condition, the exponential behaviour of the power can be approximated to a linear trend which follows the expression

$$P(z) = P(0) + P_{sat} \cdot \frac{\alpha}{4.343} \cdot z, \tag{5.4}$$

where the saturation power is given by

$$P_{sat} = \frac{A_{eff} h\nu}{(\sigma_{em} + \sigma_{abs}) \cdot \tau \Gamma_P}, \tag{5.5}$$

being σ_{em} and σ_{abs} the emission and absorption cross section respectively, A_{eff} the effective area, α designates the absorption, Γ_P is defined as the overlap factor of pump mode field with the doped area and τ is the lifetime of the rare-earth dopants which is equal to 0.85 ms. Using the above expression the absorption coefficient can be extracted at the fiber output. From the study of *Dawson et all* [47] the Ytterbium absorption and emission cross sections at 974.5 nm are $1.823 \cdot 10^{-24} m^2$ and $1.87 \cdot 10^{-24} m^2$, respectively whereas the overlap factor is defined as

$$\Gamma_P = 1 - exp\Big(- 2 \cdot (\frac{r_{core}}{r_{MFD}})^2\Big). \tag{5.6}$$

The theoretical expression of the saturation power is 2.6 mW. This simple calculation further confirms the goodness of the simulation, in fact the extracted saturation power is equal to 2.492 mW which is within the 4% of acceptable error. The slight deviation could be due to different emission and absorption cross sections used by the software.

If m is the slope of the straight line, the absorption at the fiber end is

$$\alpha = \frac{m \cdot 4.343}{P_{sat}} = 780.56 dB/m. \tag{5.7}$$

The second plot in Figure 5.1 (b) presents the signal output power as a function of the pump power. After the threshold value is overcome, the increase of the

pumping leads to an almost flat trend of the output. This implies the achievement of gain saturation condition which is reached at 0.2 W and further increase of the pumping power is pointless.

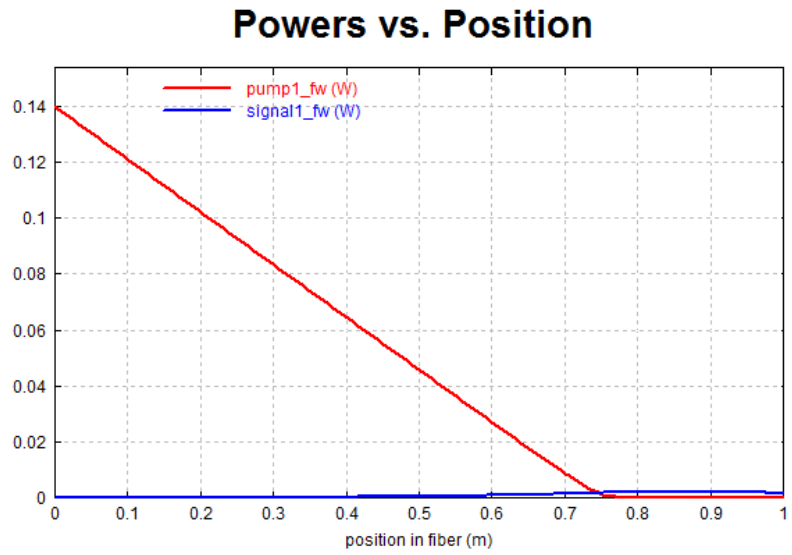

(a)

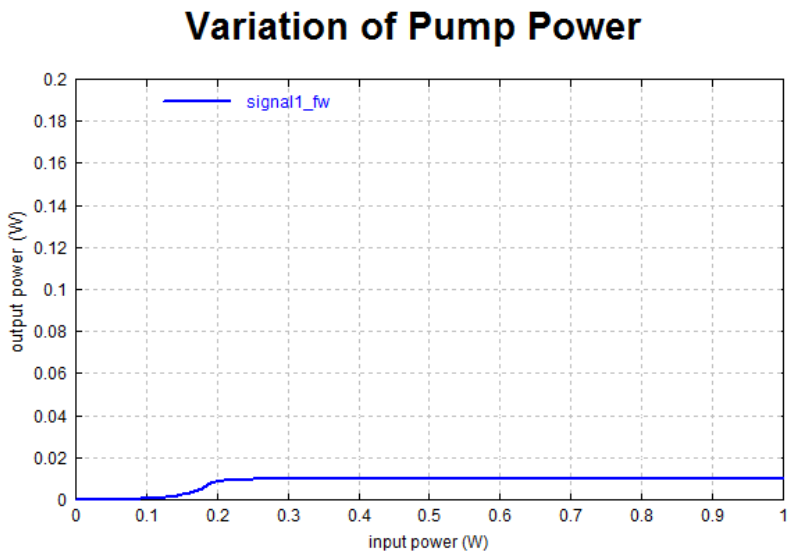

(b)

Figure 5.1: *(a) Pump and signal powers along the fiber length (b) output power as a function of the pump input power.*

Second stage Differently from the first stage, the second active fiber has been designed to be cladding pumped with a multi-mode pump module at 976 nm in backward direction. LP01 and LP11 amplify the signal by 38.4 dB and 27.2 dB, respectively. From Figure 5.2 (b) their different amplifications are clearly shown graphically: on one hand LP01 allows an output up to 12 W, on the other side LP11 reaches approximately 1.5 W. This dissimilar behaviour is justified by the amount of light intensity penetrating into the fiber, in fact as illustrated by the radial function in Figure 5.2 (a), LP11 is less focused than LP01 being the intensity spread along the fiber radius.

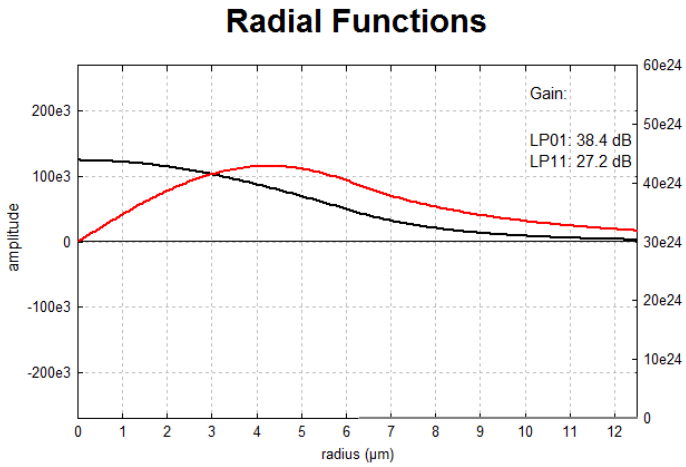

(a)

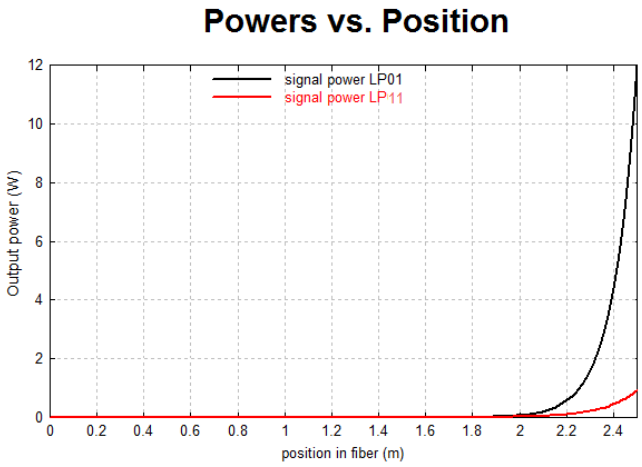

(b)

Figure 5.2: *(a) LP01 and LP11 modes as a function of the fiber radius and (b) their respective amplified output power.*

Conversely from the above case, the modelling is completely different: in fact the input signal of the amplifier corresponds to the output of the first stage. For the analyzed case an input average power of 1.74 mW has been considered, which results from the simulation of the first stage, while the pumping power was 15 W. Furthermore, the MFD is approximated to the core diameter due to the multi-mode nature of the fiber [44]. As it is plotted in Figure 5.4 (a), the signal is amplified to more than 12 W at the fiber output with a gain of 38.6 dB. Instead, the second diagram in Figure 5.4 (b) reports the linear variation of the output signal as a function of the pump power. The value of the slope efficiency for the fiber laser can be finally extracted and results 88.3 %. The simulations can be compared to the experimental results of *Novotny et all* [1] in order to create an useful reference for the characterization in the following section. As studied by the authors, the average output power varies linearly with respect to the increase of the pump power. When the latter is set to 15 W the output power is amplified to 12 W at 50 MHz repetition rate showing a slope efficiency of 87% and a gain of 30 dB. Thus, the results from the simulation can be considered satisfying and a good reference point. Moreover, in the simulations the influence of the ASE has not been investigated and this is one of the reason of the slightly mismatch with the experimental data. Theoretically, what is aspected is a decrease in the slope efficiency with the increase of the repetition rate due to the progressively appearance of spontaneous emission amplification.
Finally, an almost flat response of the output power to the signal input power growth is illustrated in the last plot in Figure 5.3. This can suggest that the performance of the first stage does not influence the final output of the fiber laser.

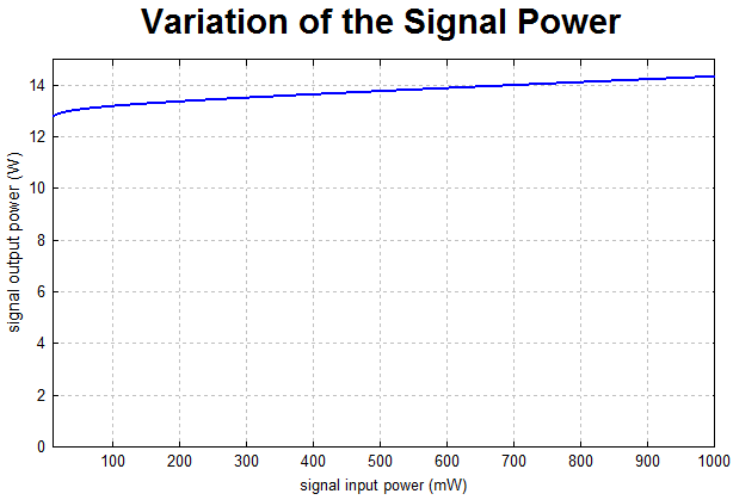

Figure 5.3: *Amplified power as a function of first stage output.*

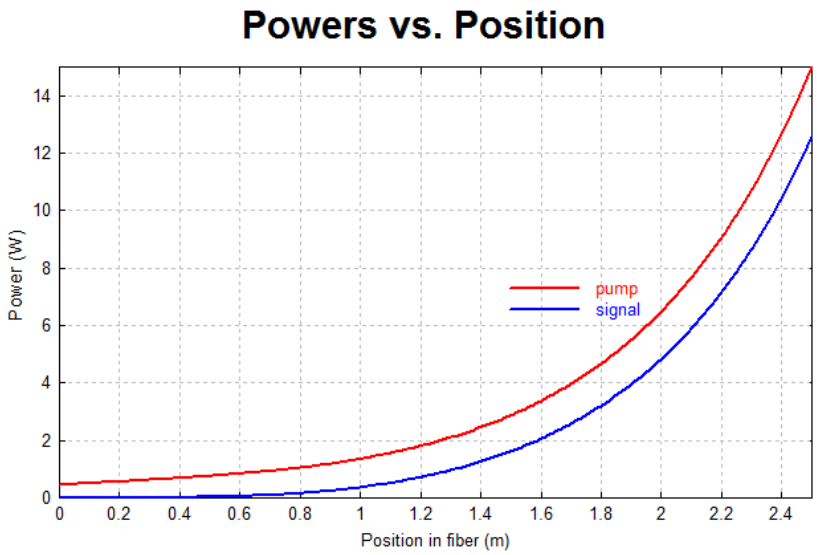

(a)

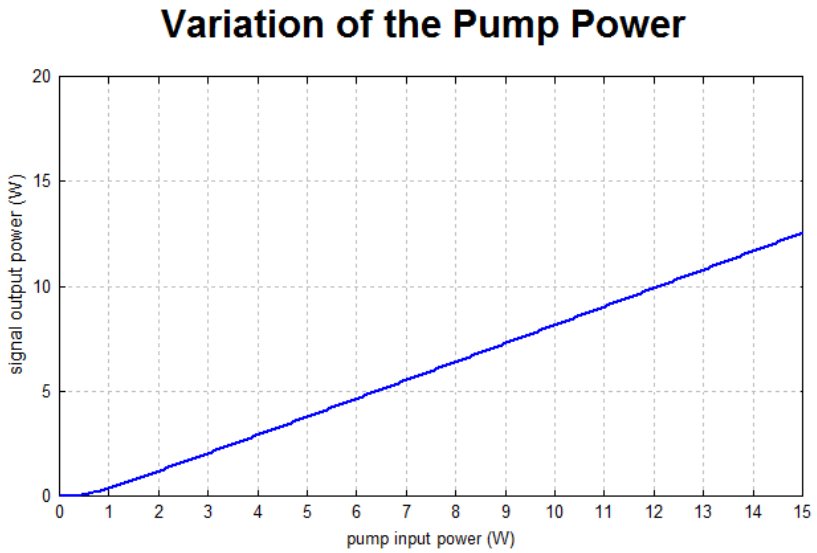

(b)

Figure 5.4: *Output power along the fiber length (a) and amplified power as a function of MM-pumping (b).*

Two-stages with ASE The overall behaviour of the two-stages amplifier has been simulated taking into account the amplification of the spontaneous emission. As in the previous analysis, the first amplifier is fed with a Gaussian pulse, which has been modeled basing on its average properties, then its output works as input for the second stage. In Figure 5.5 the output powers in both stages are reported. The results do not match with the previous ones: in the first stage the output power reaches 50 mW, compared to 170 mW of the previous analysis. A worse result is obtained for the second amplification where the output power at the end of the fiber is 1 W. This huge mismatch is due to the presence of ASE whose understanding is challenging and it might not be modelled properly. Moreover, further improvements of the model can be obtained if pulses propagation are taken into account. In fact the use of average dimensions limits the veracity of the model with respect to the real physics since effects as fiber nonlinearities are not considered. To obtain this a larger and deeper programming ability is required.

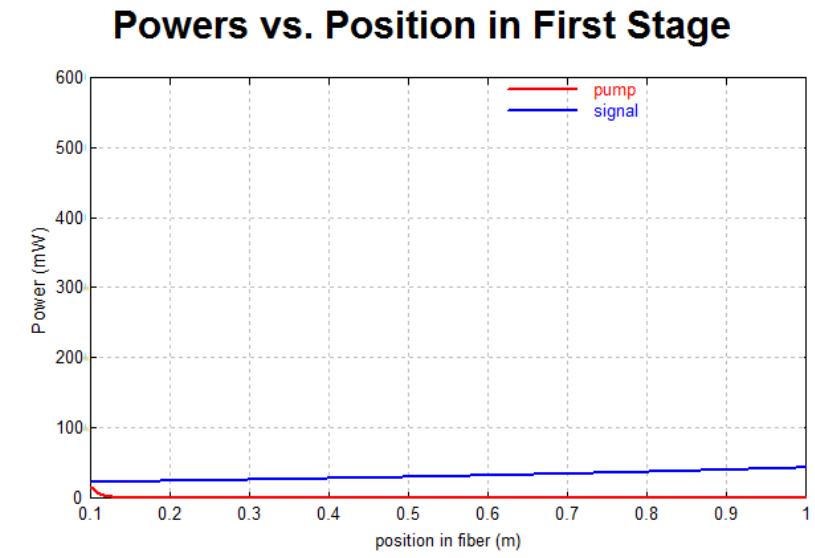

(a)

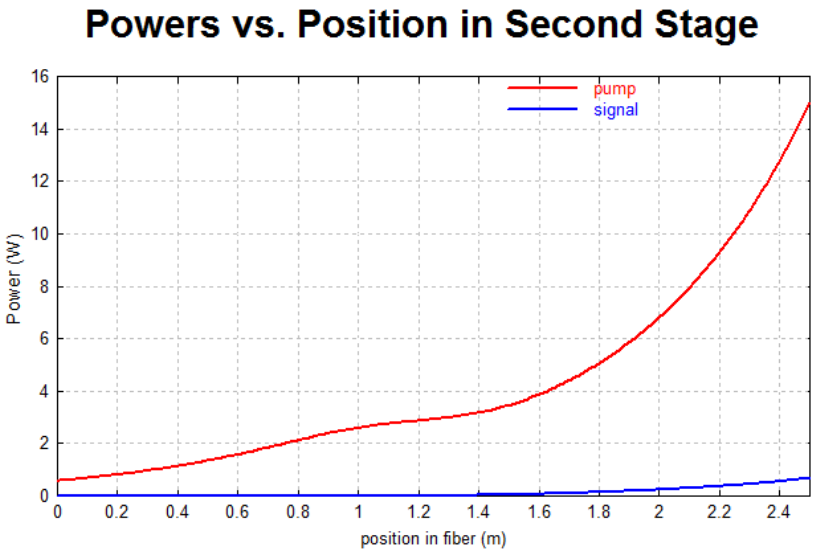

(b)

Figure 5.5: *Amplified signal along first stage (a) and second stage (b) amplification.*

Experimental characterization

The performance of the fiber laser was firstly studied in terms of average output power and peak power as a function of the second stage pumping power together with its output spectrum. Then, the spectral measurements together with pulse width and beam quality are performed. Subsequently, to assess the reliability of

the SCG the efficiency of the SHG is measured.

Output power

A 3 Watts power-meter was positioned at the output of the fiber laser, in particular immediately after the second half-wave plate and at the fiber output. The output powers at different frequencies have been sensed during the variation of the voltage setting imposed to the second stage amplifier. Consequently, a conversion from voltage setting to pumping power is required. Using the data-sheet of the power-meter the expression below was applied

$$P_{pump} = 58.5442 \cdot V - 0.7258, \tag{5.8}$$

where V is the voltage applied to the second stage amplifier.

The peak power is derived from the measured average power

$$P_{peak} = \frac{P_{avg}}{D}, \tag{5.9}$$

where D is the duty-cycle. The input pulse is characterized by the repetition rate R and pulse width D_{pulse}, thus the peak power can be written as

$$P_{peak} = \frac{P_{avg}}{D_{pulse} \cdot R}. \tag{5.10}$$

The linear trend is plotted in Figure 5.6: the repetition rate increases and a higher average power is needed to reach a given peak power.

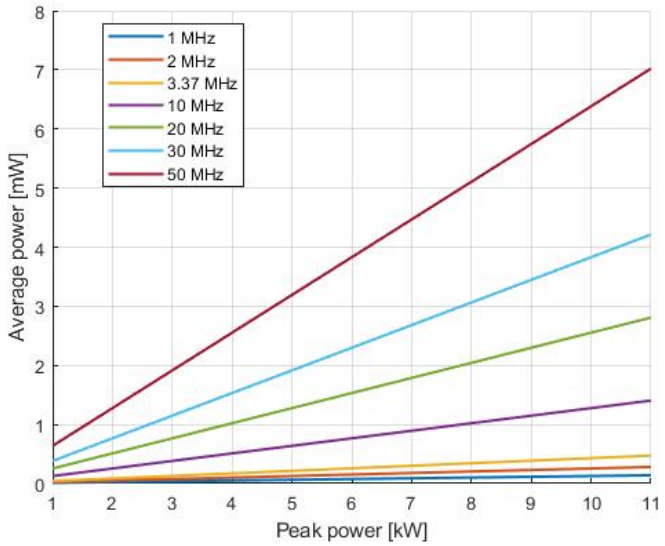

Figure 5.6: *Average output power as a function of the peak power for different values of repetition rate for a 50 ps-long Gaussian pulse.*

Assuming a 50 ps width Gaussian pulse in the continuous wave condition, the experimental results are presented in the plots of Figure 5.7. From plots (a-c), the higher the repetition frequency the greater the average output power from the fiber laser. On the contrary, plots (b-d) report that a higher peak power is reached for low repetition rate at the same pump power. The trends are linear as predicted in the simulation result shown in Figure 5.1 (b), even though a more precise fitting can be obtained if the pump power coupling efficiency for the second pump is assumed to be 94 %.

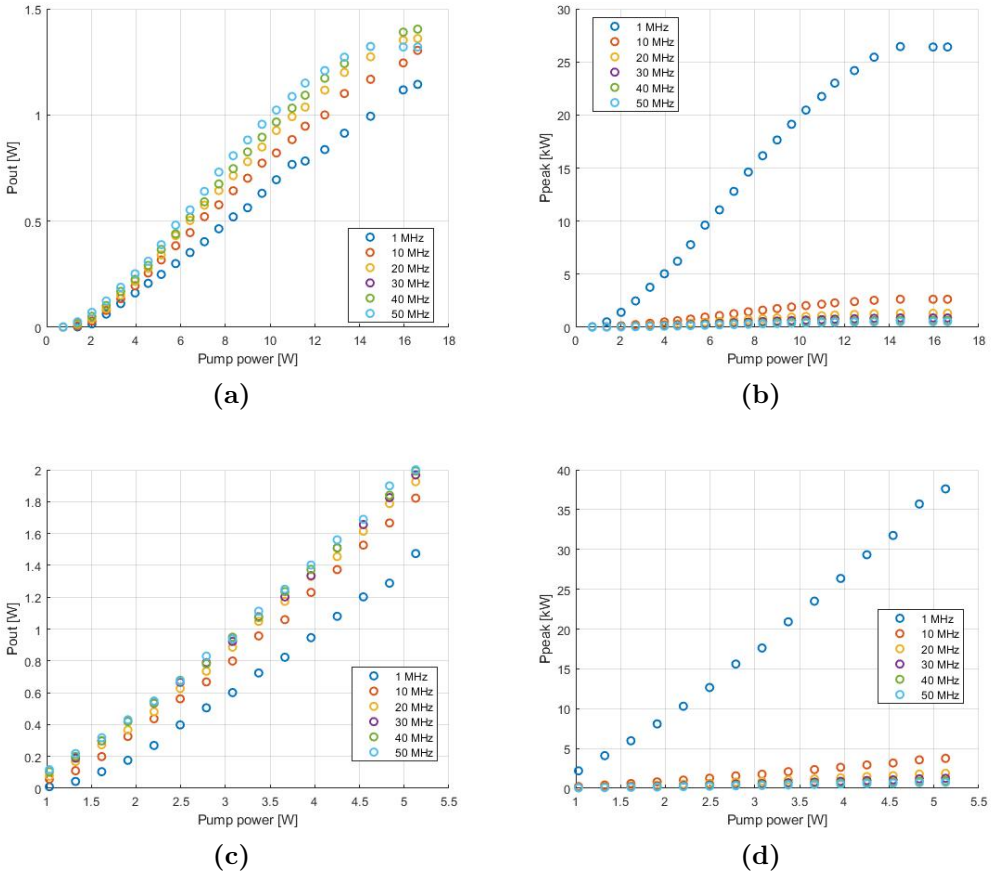

Figure 5.7: *Average output power (a-c) and peak power (b-d) as a function the the second stage pump power for different repetition frequencies after the second lambda/2 wave-plate and at the fiber output, respectively.*

The measurements sensed can be comparable with good agreement with the characterization conducted by *Novotny et al.* A satisfactory matching in the trend of peak power has been found, in fact the growth is linear as aspected and the lower the repetition frequency the larger is the peak power. The last consideration is further assess in the next section thanks to the spectral measurements.
Nevertheless, a slight deviation in the average output power is present. Probably the latter is strongly affected by the fluctuation of the pump power which is not stable. Additionally, the performance can be also influenced by the splicing between the active and passive fiber. In fact, due to the polarization maintaining nature of the fiber splicing is a very delicate operation requiring surgical precision in the alignment and if it is not done properly it could affect remarkably the loss. Despite this, both the trend and the data collected are coherent with respect to the past characterization as already stated. Thus, these results allow to highlight what previously mentioned: one advantage of fiber laser is the huge output power at relatively low input current and the performed analysis confirms what stated in [31] - [33] - [32] - [29]. An input voltage of ≈ 70 mV is sufficient to generate average power of 2 W at 50 MHz repetition rate.

Spectrum

The spectra of the fiber laser for different repetition rates have been recorded using OceanOptics spectrometer [48]. Figure 5.8 reports the laser output for 1, 10, 20 and 50 MHz. At a low repetition rate, the spectrum presents one main peak at $\approx 1064nm$ and two others at lower wavelength. If the frequency of repetition increases, the intensity of the main peak grows reaching almost $15kW$ of power. Moreover, the lateral peaks disappears and the main peak broaders. This is basically a consequence of the conservation of energy.

In principal, the spectral analysis allows the calculation of the pulse length L by using the following formula

$$\frac{P_{avg}}{P_{peak}} = 20log_{10}(L \cdot f), \tag{5.11}$$

where f is the frequency [49].
Albeit, the results are absolutely unsatisfactory and span in the order of nanoseconds. This flop was aspected since the spectral analysis gives rough results for this purpose. The proper way to characterize the pulse duration is the combination of a photodiode and an oscilloscope, as described in the next section.

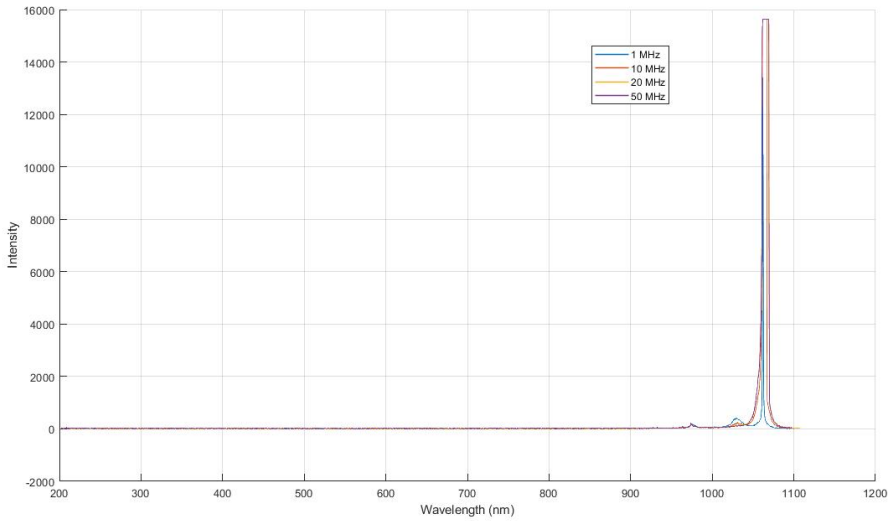

Figure 5.8: *Fiber laser spectrum for different repetition rates.*

Gaussian beam characterization

One of the simplest approach for a laser beam characterization is to treat its output as a Gaussian beam. In fact, due to its simplicity, the temporal and spatial evolution is easily predictable.

The amplitude distribution of a 2D Gaussian beam propagating toward the traversal direction x and the axial direction z follows the expression [50]- [51]

$$\Psi(x,z) = \Psi_0\sqrt{\frac{2}{\pi}}\frac{\omega_0 exp[-i(\phi_0 - \phi(z))]}{\omega(z)} \cdot exp\Big[-i\frac{kx^2}{2R(z)} - \frac{x^2}{\omega^2(z)}\Big]. \tag{5.12}$$

As shown from the above equation, the amplitude has both real and imaginary components, in particular:

- $\Psi(x,z) \approx exp(-\frac{x^2}{\omega^2(z)})$ is imaginary and is associated to the phase of the beam.
- The square modulus of the amplitude is defined as irradiance which is a real function. Its transversal distribution is represented by $I(x,z) = |\Psi(x,z)|^2 \approx exp(-\frac{2x^2}{\omega^2})$.

The function $\omega(z)$ is the beam width and represents the transversal beam extension during its propagation. In particular it describes the evolution of all points having a decrease of $1/e$ in amplitude (or $1/e^2$ in irradiance) and its expression is

$$\omega(z) = \omega_0\sqrt{1 + \Big(\frac{z\lambda}{\pi\omega_0^2}\Big)^2}. \tag{5.13}$$

where ω_0 is defined as the minimum value of the beam and it is named beam waist.

If the lower and upper boundaries at $\pm\infty$ respectively are considered, the divergence angle of the beam is found

$$\theta_0 \approx tg\theta_0 = \frac{\lambda}{\pi\omega_0}, \tag{5.14}$$

which represents the spread of the beam along its propagation direction and it is correlated to the width. From the divergence, consideration concerning the goodness of the collimation and focusing can be stated

- Good collimation when the beam is wide, means low θ.
- Good focusing when θ is large, meaning low ω.

The imaginary part of Equation 5.12 is squared x-dependent

$$exp\Big[-i\frac{kx^2}{2R(z)}\Big], \tag{5.15}$$

and is the mathematical expression for a spherical wavefront with radius $R(z)$. This parameter is useful to detect the curvature of the associated wavefront which follows the expression

$$R(z) = z\Big[1 + \Big(\frac{\pi\omega_0^2}{z\lambda}\Big)^2\Big]. \tag{5.16}$$

Since width, divergence and radius depend on both the wavelength and ω_0, a parameter called Rayleigh range z_R is defined for describing the extension of the beam towards its propagation direction. Its expression is

$$z_R = \frac{\pi\omega_0^2}{\lambda}. \tag{5.17}$$

Finally, in Equation 5.12 there is another term related to the phase shift which is defined as

$$\phi(z) = tg^{-1}(\frac{z}{z_R}). \tag{5.18}$$

This explains the phase shift of π every time the front crosses the beam waist region and it is known as Guoy phase shift.

Despite all the advantages of the Gaussian treatment, only the TEM_{00} mode can be considered truly Gaussian. For this reason a parameter, called quality factor M^2, has been defined to monitor the laser beam deviation from the theoretical Gaussian shape and allows for comparison between beams. This means that:

- if $M^2 = 1$ the beam is truly Gaussian and it is used as a reference of quality for a laser source;
- if $M^2 < 1$ it is not physical acceptable;
- if $M^2 > 1$ real value lasers. In general, ion lasers are in the range 1.1 to 1.3, diode laser from 1.1 to 1.7 and helium neon lasers have a quality factor lower than 1.1. The higher the value of M^2 the worse the quality of the beam, meaning not satisfactory performance during collimation and focusing;

Since the studied setup is hybrid, which means that Gaussian beams interact with optical components, the matrix method can be applied. The latter is a mathematical approach widely used in optics which allows to describe the effect of an optical system on a light ray through a cascade of matrixes. Light is described as a ray characterized by height x_i and angle α_i wrt the optical axis of the system whereas the optical system is represented by a 2x2 matrix named ABCD matrix. For istance, if $\vec{x_1}$ is the incoming ray the output ray $\vec{x_2}$ after the transformation imposed by the optical system is

$$\begin{Bmatrix} x_2 \\ \alpha_2 \end{Bmatrix} = \begin{bmatrix} A & B \\ C & D \end{bmatrix} \begin{Bmatrix} x_1 \\ \alpha_1 \end{Bmatrix}. \tag{5.19}$$

This method is particularly useful in the beam quality characterization.

Temporal pulse width measurement As already stated above, the duration of the optical pulse is sensed with a photodiode and an oscilloscope. Pulse duration is determined by viewing the laser output on the oscilloscope and applying the full-width-half-maximum (FWHM) criteria.

The output of the fiber laser is collimated by a collimator with NA=0.15 and focal length 18.4 mm. If one applies Equation 5.22, a rough comparison with the pulse width measured can be done. Indeed, from the practical calculations the amplified pulse has a width of 310ps if the input pulse is 50 ps. The measured pulse width is 340ps for 1 MHz repetition rate and $P_{pump,2} \approx 2W$. Consequently, the pulse width measurements are consistent and reliable. It is important to mention that the measure is affected by numerous parameters such as: position, pump power, repetition rate, type of oscilloscope and optical setup alignment. In particular the latter plays a relevant role since it determines the eventual loss of transmitted signal. Moreover, what could have affected the entire setup is the splicing between active and passive fibers. The alignment could be not perfectly matched and this could contribute to further loss and broadening of the signal.

Beam quality M^2 The beam quality and its deviation from the Gaussian shape are checked through M^2 measurements using Ophir Beamstar software [52].

The standard ISO-11146 defined M^2 as

$$M^2 = \frac{\pi}{\lambda}\frac{d_{\sigma 0}\theta_\sigma}{4}, \tag{5.20}$$

where λ is the laser beam wavelength, $d_{\sigma 0}$ the real waist diameter and θ_σ the divergence angle. At this point, according to Equation 5.20 one must compute and measure the elements needed for the calculation of the quality factor. The steps can be summarized as follow:

1. The wavelength is known.
2. The divergence angle, which is an invariant, must be computed according to

$$\theta_d = \theta_\sigma = \frac{d_{\sigma f}}{f}, \tag{5.21}$$

where f is the focal length of the focusing element and $d_{\sigma f}$ is the beam width at one focal length away from the rear principal plane of the focusing element. Thus, the beam width at the focal length must be sensed [1].

[1]Since the beam does not converge outside the laser cavity, the direct measure of the true waist diameter $d_{\sigma 0}$ is a challenging task. To simplify measurements a focusing element is set in front of the light source. The measure from this alternative solution is called artificial beam waist $d_{\sigma f}$.

3. The beam waist $d_{\sigma f}$ is found by moving the detector along the laser's path and look for the minimum.

4. Apply Equation 5.20.

The measurements are not straightforward because of many error sources as inaccurancy in the z-position, aberration of the focusing element, inaccuracy of the measurement device and wrong focal lenght. For these reason the measurements are taken in slots: at least 5 measurements of the z-position within at least two Rayleigh length (far field condition) and at least 5 measurements within one Rayleigh range (near field condition) are needed.

Light emitting from a fiber typically has a high divergence angle. For this reason the setup illustrated in Figure 5.9 was used. Light from the laser source at wavelength λ is firstly collimated through a lens having focal length f, then it is focused by another lens with focal length of f'.
The choice of the optical components is fundamental for a successful characterization of the Gaussian pulse. One condition to be full-filled is to have the ratio between focal length of lens and diameter of the collimated beam at the lens surface above 20. Having suppose that the mode field diameter of the laser is y_1 and NA was named θ_1, the image created will be characterized by a divergence angle θ_2 and radius r_2 determined by the following formula

$$y_2 = \theta_1 f \quad and \quad \theta_2 = \frac{y_1}{f}. \tag{5.22}$$

The beam will travel and reach the focusing lens. At the lens output the beam is characterized by

$$y_3 = \theta_2 f' \quad and \quad \theta_3 = \frac{y_2}{f'}. \tag{5.23}$$

From the above equations, the focused beam waist depends on the focal lengths of both collimating and focusing lenses according to

$$\frac{f'}{f} > \frac{NA}{20} \approx 0.004, \tag{5.24}$$

which highlights the importance of the appropriate optical components.

To compute the real waist diameter $d_{\sigma 0}$, it is necessary to measure the artificial waist $d_{\sigma f}$ first according to the *step*3. The latter is used to compute the Rayleigh length according the formula

$$z_R = \frac{\pi}{\lambda} d_{\sigma f}. \tag{5.25}$$

Finally, knowing by definition that the Rayleigh length is the distance at which the beam width increases by a factor $\sqrt{2}$ the true waist diameter is computed

$$z_R = \sqrt{2} d_{\sigma 0}. \tag{5.26}$$

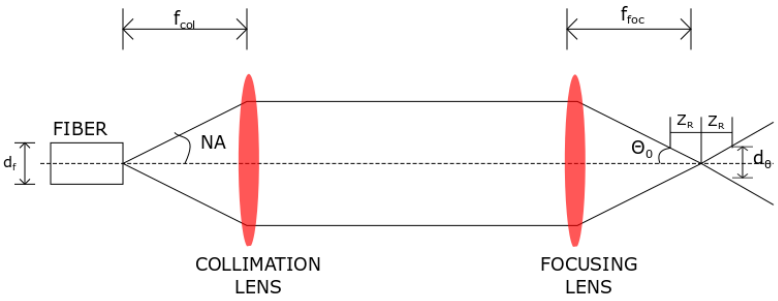

Figure 5.9: *Experimental setup for quality factor M^2 measurements.*

Fiber lasers have a low M^2 value and there exist devices commercially available with a beam quality lower than 1.2. Unfortunately, the value obtained from the experiment is too large and overcomes 2. The reason behind this huge error is not to be attributed to the bad quality of the beam since both the width and output power measurements are satisfying. It is more probable that the measurements must be performed with more attention and precision, in fact carefulness is fundamental for a successful characterization of the quality beam. Moreover, a more appropriated camera could be used in order to improve the measurement results.

5.1.1 Second harmonic generation

The software *COMSOL Multiphysics*© [39] has been used to simulate the generation of the second harmonics. The geometrical model consist in a simple rectangle with one mesh element in the perpendicular direction to the propagation axis. Both the fundamental signal and the second harmonics have been modelled as electromagnetic waves in the frequency domain at f_1 and $2f_1$ frequency, respectively. The fundamental mode is polarized in the y direction and impinges on the geometry through a Scattering Boundary Condition feature. The two waves are coupled at both interfaces by a polarization feature, knowing that the two polarizations are

$$P_{1,y} = 2dE_{2,y} \cdot E^*_{1,y}, \tag{5.27}$$

$$P_{2,y} = d \cdot E_{1,y} \tag{5.28}$$

where d defines the nonlinear coefficient for the process, $E_{1,y}$ and $E_{2,y}$ are the y-component of the electric field at the fundamental and second harmonic frequency, respectively [53].

Figure 5.10 shows the electric field along the y of the fundamental mode and second harmonics. As aspected the amplitude of the former is decreasing during the propagation, leading to the energy transfer to the second harmonics. As a result, its amplitude grows maintaining the conservation of energy among the overall system.

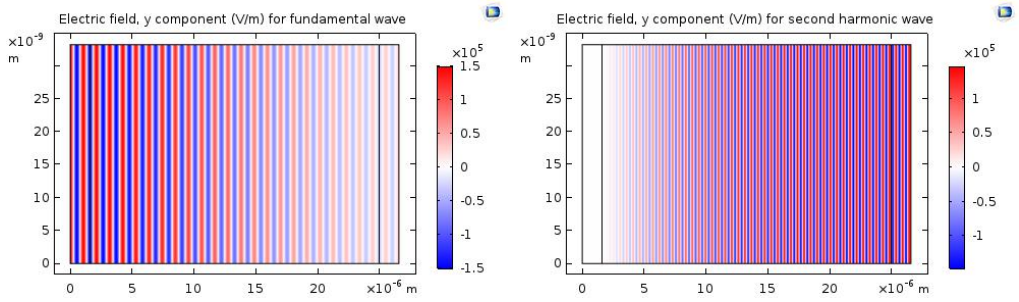

(a) Fundamental **(b)** Second harmonics

Figure 5.10: *Electric field along y axis for (a) fundamental mode and (b) second harmonics.*

The efficiency of the second harmonic generation has been defined as follows

$$\eta_{SGH} = \frac{P_{1064} \cdot t_{1064} + P_{532} \cdot t_{532}}{P_{tot}}, \tag{5.29}$$

having assumed that

- The repetition rate has been set to 1 MHz;
- The transmission t_{532} of the 532nm filter is 0.67;
- 1064 nm filter has a transmission t_{1064} of 0.83;
- The Gaussian pulse is supposed to have a width of 50 ps.
- The second pump power coupling efficiency is 0.94.

The 3 Watts power-meter has been placed after the KTP crystal in order to measure firstly the power P_{1064} and P_{532} with 1064 nm and 532 nm filters respectively and lastly the total power.
The results are reported in Figure 5.11: the efficiency lays in the range from 2.5 to 3.5. The trend is characterized by many fluctuations, even if as a general consideration it is almost steady if the pump power is increased.

If the results are compared to the work of *Novotny et al.*, the values of efficiency obtained are three times lower. The power loss of the fiber laser due to a non-perfect splicing is not the principal cause of this result. In fact, as already stated in the previous section, despite the splicing loss the laser output does not deviate from the range of acceptable error. What strongly influences the second harmonic generation is the alignment of the optics setup and the position of the KTP crystal. Such a low efficiency value suggests the need of better coupling in order to reach higher output power.

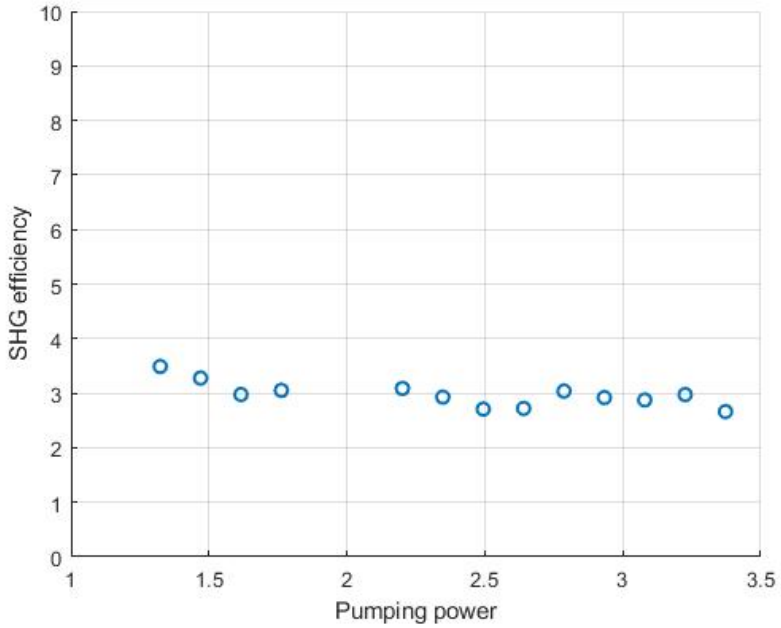

Figure 5.11: *SHG efficiency as a function of the second stage pump power.*

5.1.2 Supercontinuum generation

The gain-switched fiber laser generates picosecond pulse train, consequently the expectation is that the SC is generated by the following nonlinearities depending on the dispersion condition: FWM, Raman scattering, SPM, MI, dispersive wave and Raman induced soliton self frequency shift. The two signals at 1064 nm and 532 nm lie in anomalous and normal dispersion region, respectively. Therefore, in the IR region the spectrum should show modulation instabily, dispersive wave and soliton shift. On the contrary when the VIS signal is considered, FWM, Raman scattering and SPM should be the cause of the spectral broadening.

Modelling and simulations of the supercontinuum generation

Simulations using an implemented code basing on [54] were run. Mathematically, the pulse launched into the fiber propagates according to the solution of the NLSE Equation 2.6. In the equation, left-hand side takes care of the linear propagation effects such as dispersion and attenuation whereas the right-hand side models nonlinearities.

The code solves the following NLSE which has been re-written neglecting both the frequency-dependency of n_2, n_{eff} and A_{eff} and losses

$$\frac{\partial \tilde{A}'}{\partial z} = i\frac{\gamma\omega}{\omega_0} exp(-\hat{L}z)\mathcal{F}\Big\{A(z,T)\int_{-\infty}^{\infty} R(T')|A(z,T-T')|^2 dT'\Big\}, \tag{5.30}$$

where $R(T')$ is the convolution integral of the Raman response given by

$$\begin{aligned}\int_{-\infty}^{\infty} R(T')|A(z,T-T')|^2 dT' &= (1-f_R)|A(z,T)|^2 \\ &+ f_R\int_{-\infty}^{\infty} h_R(T')|A(z,T-T')|^2 dT'.\end{aligned} \tag{5.31}$$

The first term represents the Kerr optical effect, while the second term is the convolution integral referring to the stimulated Raman scattering. Exploiting the convolution theorem the latter is numerically evaluated solving the following expression [54]

$$\int_{-\infty}^{\infty} h_R(T')|A(z,T-T')|^2 dT' = \mathcal{F}^{-1}\Big[\mathcal{F}(h_R(T))\mathcal{F}(|A(z,T)|^2)\Big]. \tag{5.32}$$

Normal dispersion The code simulates the spectrum evolution of a Gaussian along 15 cm and 1 m long fiber. The pulse width is 45 ps with a peak power of 15kW at 1 MHz repetition rate, which results from the previous fiber laser characterization. As shown in Figure 5.12 (a), the pulse propagates within the first fiber centimeter, then an asymmetrical broaden spectrum spanning from 400 nm to 1000 nm appears and it is maintained till the fiber output.
Noise perturbs the pulse leading to modulation instability, thus it breaks up the pump and generates solitons. After 2 cm the spectrum broadens due to self-phase modulation, Raman scattering and, as stated in [55], the group delay properties of the fiber. The spectrum continues to extent toward the blue region as a results soliton shift induced by the Raman gain. If the pulse propagation is observed toward a longer fiber, as reported in Figure 5.12 (b), higher order blue-shift solitons appear. Differently from what aspected, FWM is not observed. The main reason could be the distance of the pumping wavelength to the ZDW, in fact if they are not close enough the Raman gain predominates over the four-wave mixing process.

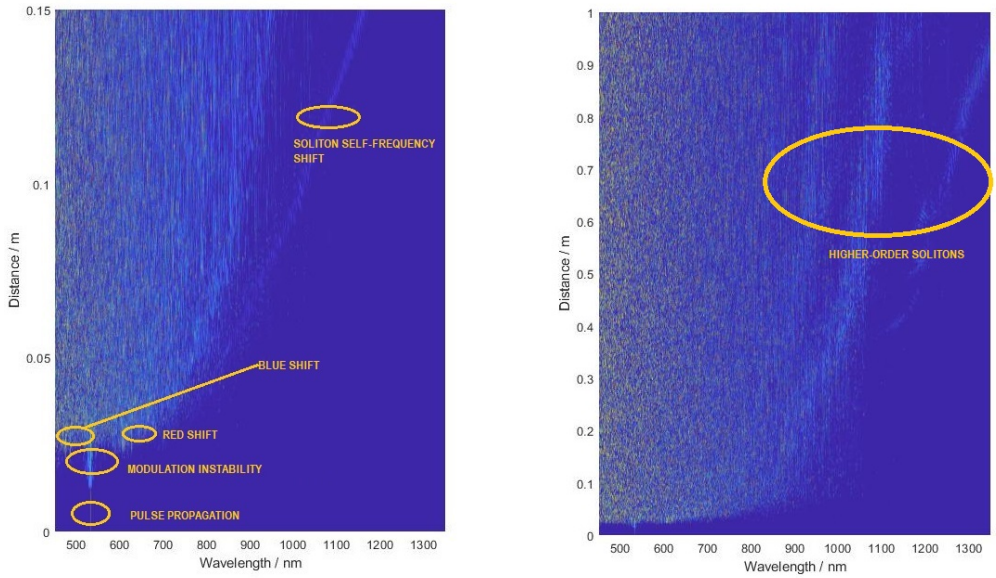

(a) **(b)**

Figure 5.12: *Pulse propagation along (a) 15cm long and (b) 1 m long fiber at 532 nm pumping wavelength.*

Anomalous dispersion Conversely from the previous case, the spectrum generated is wider and symmetrical. In particular, its extension spans from 400 nm to 1400 nm covering both the visible and the infrared regions.

Under anomalous dispersion condition, the mechanisms behind SCG are solitons-based and usually named as *soliton dynamics*. Indeed, when high peak power pulses are injected into a high nonlinear fiber in the anomalous condition, the associated soliton number (Equation 2.24) is huge and, consequently, their contribution to SCG is great. As shown in Figure 5.13, the initial modulation instability builds higher order solitons which broaden the spectrum and compress the pulse. However, they are intrinsically unstable and if perturbed a break up into sub-pulses is manifested. In this case, higher-order dispersion effects induce the energy transfer from the soliton to a narrow band resonance energy leading to a broadening effect towards the blue side. This phenomenon is known as dispersive wave. Finally, the overlap between solitons and Raman gain induces a solitons self-shift which further widens the spectrum.

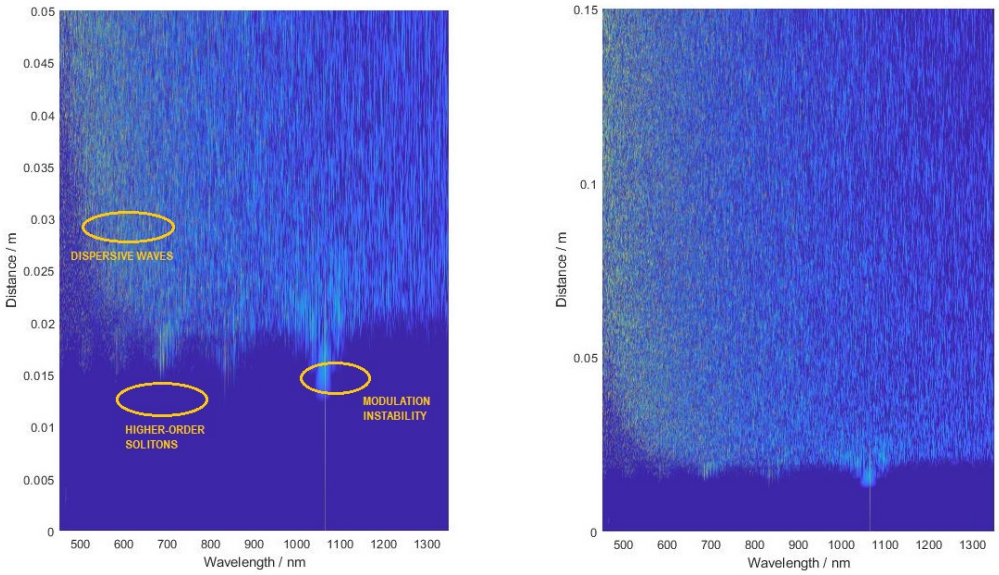

Figure 5.13: *Pulse propagation along (a) 5cm long and (b) 15 Cm long fiber at 1064 nm pumping wavelength.*

Notwithstanding the reasonable agreement with theoretical studies, the code presents few limitations which can be improved. Firstly, only one pump setting is available in contrast to the dual-pumping scheme of the experimental setup. This could be the reason for the absence of XPM in the normal dispersion condition. In fact, as demonstrated from the studies conducted by *Novotny et al.*, the blue-shift in the visible region is caused by cascade cross phase modulation which rises from the interaction between the visible pump wave and the IR solitons [1]. Due to the absence of the infrared pumping this in not observed, moreover it justifies another incoherence of the simulation. MI should occur only in the anomalous region as effect of the balance between the negative chirp induced by GVD and the positive chirp of SPM.

Albeit the same input pulse was assumed, the spectral broadening is different in the two cases which highlights the importance of the dispersion condition on the SCG. As stated in the previous considerations, in the IR region the spectrum is broader than in VIS region. Many studies [55] [56] demonstrated that the closer the pumping wavelength is to the zero-dispersion wavelength the larger is the bandwidth. However, this does not justify the different spectral width since both the pumping wavelength are equally distant from the ZDW. The differences are explained by the dissimilar values of group-velocity dispersion. Dispersion in

normal condition is higher than in anomalous. This means that the components in the IR regions are subjected to a larger blue-shift than the ones in the VIS. In other words, the visible continuum covers the wavelengths that are group-delay matched with the infrared continuum [57]. Therefore, from these considerations the importance of dispersion is further emphasized. It is important to consider not only the sign of dispersion, which affects the mechanisms behind the generation, also its magnitude strongly influences both the extension of the spectrum and type of broadening (blue/red shifts).

Finally, simulations with longer fiber can be run and a wider spectrum is aspected since the strength of nonlinearities are proportional to the product of the power and the interaction length [6]. Albeit, it is computationally heavy and it takes longer.

Spectral results

The simulations implemented in the previous section help in the interpretation of the spectral analysis. Differently from what numerically simulated, the broad spectrum has been generated under dual pumping condition and this is the reason for modest discrepancies. As already mentioned above, when a MOF is pumped with short pulses around 1060 nm the dominant nonlinear effect is Raman scattering which causes the enlargement towards the infrared region only. In order to obtain the spectral broadening at lower wavelength, a dual-pumping is applied thanks to the second harmonics generation obtained from the optical components of the setup.

Figure 5.14 shows the spectrum of the supercontinuum for two different peak powers at 1 MHz repetition rate in the IR region. At long wavelength the spectral spreading is initialized by solitons dynamics. This is clearly demonstrated by the peak at 1064 nm which enlarges due to modulation instability till 1350 nm. Moreover, if the peak power increases a higher gain and slightly broader spectrum is obtained. In fact, as predicted from simulations under higher pumping power solitons start to self-shift towards longer wavelength. Albeit, a better broadening can be obtained. The polarization maintaining nature of the active fiber helps the maximization of the spectrum, nevertheless an improvement in the optics alignment must be performed in order to obtain higher output power. Comparing with the results obtained by *Novotny et al.*, if on one hand the maximum broadening is reached, on the other the gain is low. The latter can be improved by reaching both a better coupling of the light into the MOF and an optimum alignment of the KTP crystal and optics components.

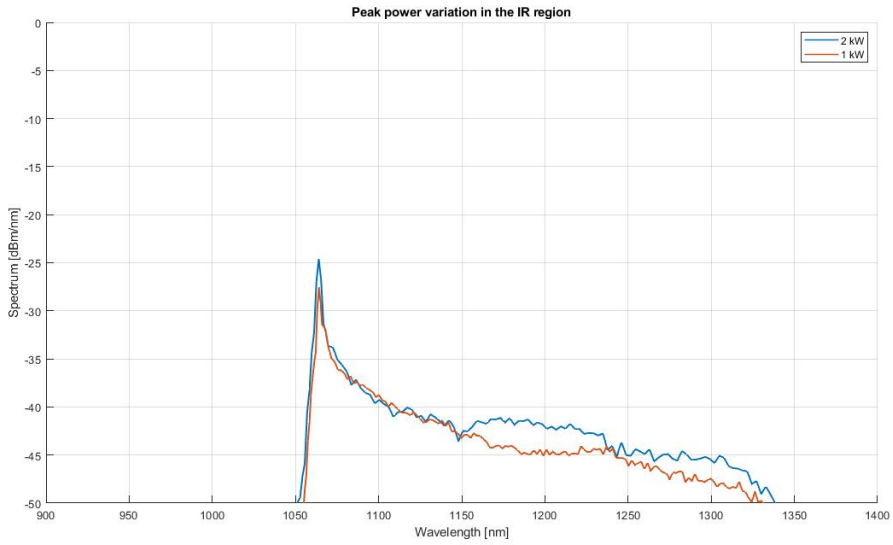

Figure 5.14: *Supercontinuum generation in the visible region at different peak powers.*

The spectral evolution in the visible region, reported in Figure 5.15 at different peak powers, allows the recognition of different nonlinearities in particular those ones which could not be modelled numerically.
When the input power is low, the peak of 532 nm pumping power is visible. Then, if the peak power increases, the pump starts interacting with infrared solitons which born from the 1064 nm pumping. This process is to be interpreted as four-waves mixing which generate further peaks along the red side. These peaks start propagating and influence each others leading to a cascade cross phase modulation process. The higher the peak power is, the flatter the spectrum becomes since nonlinear effects are strongly enhanced.

If on one hand the experimental results highlights the presence of FWM which could not be modelled, on the other hand no signal is detected below 500 nm. In fact according to what predicted in the simulations and what obtained from *Novotny et al.*, a blue-shift caused by Raman scattering was aspected. Moreover, the spectrum does not show any plateaux and peaks are still present when 4 kW of peak power is reached.

This behaviour is not unexpected. In fact, it can be considered as the drawback of this setup since it is based on the generation of the second harmonics. If the efficiency of the latter is not properly maximized, a stable supercontinuum in the visible region is not guaranteed. Furthermore, the pumping at 1064 nm is not stable and consequently during the SHG this instability is strongly enhanced.

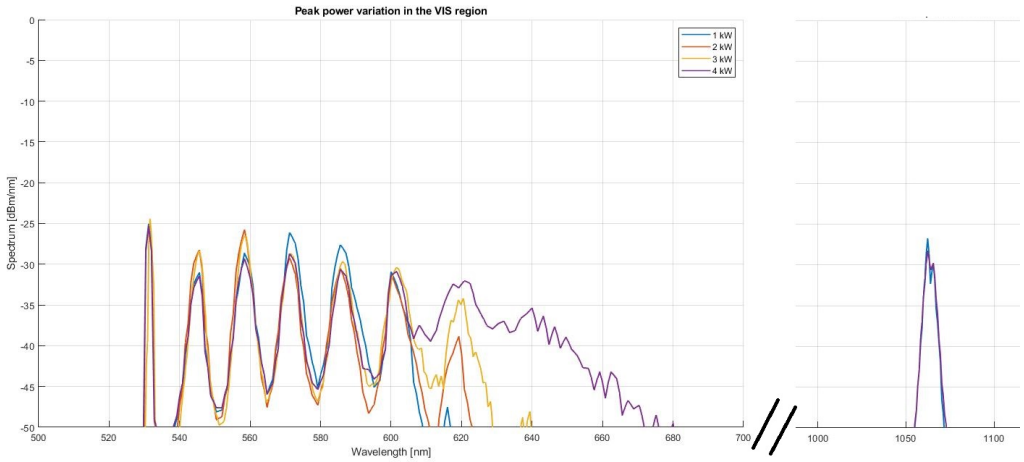

Figure 5.15: *Supercontinuum generation in the infrared spectral region at different peak powers.*

Summary

The objective of this thesis was to characterize the performance of a high power gain-switched Ytterbium-doped fiber laser used as supercontinuum light source. The laser source allows the emission of picosecond optical pulses at different repetition rates obtained by combining the light emitted from a gain-switching laser diode and all-fiber design two-stages Ytterbium-doped amplifier. The characterization is given in terms of output power, pulse width, output spectrum and quality factor.

Generally, a good correspondence between the obtained results and previous studies conducted by *Novotny et al* has been found.
The experimental results of the output power were compared with numerical simulations run using the software RP Fiber Power. Even though a more detailed modelling of the physics could be conducted, e.g. introducing a reasonable source of ASE, an optimum correlation was obtained. Good spectral properties have been assessed together with an acceptable value of beam width. Instead, the computed value of beam quality is unsatisfactory and more accurate measurements are suggested to guarantee a lower value of M^2.

If the laser output is launched into a micro-structured optical fiber a supercontinuum is generated. The broad spectrum extends both in the visible and infrared regions thanks to the frequency-doubling performed by a free-space optics setup. The flatness and width of the spectrum strongly depend on the efficiency of the second harmonics generation. Unfortunately, the latter is low and causes the presence of numerous peaks in the visible range. A better alignment of the free-space optics would increase the SHG efficiency and generate a flatter spectrum.

Additionally, the NLSE was numerically solved to identify the involved nonlinearities. Despite some limitations present in the code, the results proved to be a reliable benchmark.

Finally, the stability of the pumping can further improve the quality of the supercontinuum; for this reason an electronic control of the pumping is suggested.

Laser principle

Lasers are devices based on light amplification of stimulated emission of radiation. They differ from the other light sources thanks to their spatial and temporal coherence. Additionally, they are able to emit a focused beam which is characterized by a narrow emission spectrum.

A briefly review of the light-matter interaction is necessary. When photons with energy $E_{ph} \approx E_{gap}$ impinge on a semiconductor device the following three band-to-band processes can occur.

- Absorption: the photon is absorbed generating an electron-hole pair. The electron has sufficient energy to be promoted from the valance band to the conduction band.
- Spontaneous emission: the relaxation of the electron from the conduction band to the valance band generates the emission of a photon.
- Stimulated emission: in this process an initial incoming photon stimulates the coherent emission of another photon with the same frequency and wavevector of the incident one.

Spontaneous and stimulated emission are competitive mechanisms, consequently if the latter must be dominant a frequency-selective structure is required. For this purpose, lasers adopt optical cavities which provide temporal coherence and operate as positive feedback which is a fundamental mechanism for the predominance of the stimulated emission. In fact, it reflects back the emitted photon until the increase of the photon density in the cavity reaches the threshold value or, equivalently, the stimulated lifetime becomes smaller than the spontaneous lifetime [58]. This condition is known as *population inversion* or Bernard-Duraffourg condition, since the population density in the excited state is larger than the one of the ground state.

This is mathematically shown by the expression of the net gain G which is

$$G = g - \alpha \approx N_{cv}(f_e + f_h - 1), \tag{33}$$

where g is the gain, α the absorption, N_{cv} represents the JDOS and f_e and f_h are the Fermi-Dirac distribution for electrons and holes, respectively. The net gain must be positive for lasing operation, which means

$$f_e + f_h - 1 > 0, \tag{34}$$

implying

$$E_{F,e} - E_{F,h} > E_g, \tag{35}$$

where $E_{F,e}$ and $E_{F,h}$ are the Fermi levels of electrons and holes, respectively.

Fabry-Perot cavity

From a practical point of view, this configuration is the simplest design available since it is composed by a waveguide having two reflective facets. The waveguide posses an active region in which generation processes occur if a current is injected into the structure. Therefore, thanks to the generation of electron-hole pairs both gain and photon emission are possible. Although, only a portion of injected carriers is able to generate electron-hole pairs and this is accounted through the injection efficiency η_i. Furthermore, the lasing point is reached only for certain condition of injected current and consequently of photon density. In fact, on one hand as carriers build up in the intrinsic region gain over a certain energy interval will increase. In contrast, losses hamper the pursuit of the threshold condition: photon losses are caused by the absorption in the cladding (α_i) and mirror effects (α_m) which are essential to couple the laser source to an external waveguide. The lasing condition is reached when gain balances losses and this allows the self-sustenance of the cavity modes. Moreover, the corresponding stimulated lifetimes will decrease and the number of carriers recombined by stimulated emission increases. Nevertheless, as illustrated in Figure 16, above threshold carriers density is clamped as well as the gain since the number of injected carriers is approximately equal to the number of generated photons.

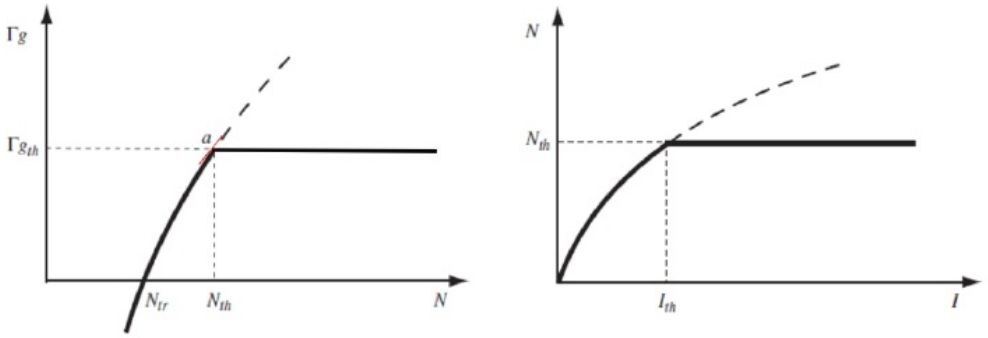

Figure 16: *[Left] Gain as a function of carrier density [right] carrier density versus input current: once the threshold condition is reached the gain is clamped since the carrier density inside the cavity is under saturation [59].*

From a mathematical point of view, the device lases only when the *round trip condition* is satisfied. Therefore after a round-trip in the cavity the optical wave must recover both the initial phase and amplitude.

Figure 17: *Rountrip of a Fabry-Perot cavity.*

To obtain a mathematical expression for the lasing, the path of a transverse electric field is followed inside a cavity composed by two mirrors having reflectivities r_1 and r_2, respectively. The mirror power reflectivity defined at normal incidence by the refraction index step with respect to air is

$$r = |R|^2 = \left(\frac{n_r - 1}{n_r + 1}\right)^2. \tag{36}$$

As sketched in Figure 17, the propagation starts from **1** and ends in **5**.

1. At the beginning of the propagation the field is expressed by E_0.

2. After being reflected the amplitude turns to be $r_1 E_0$.

3. The wave travels through the entire length of the cavity experiencing attenuation, gain and a phase shift. Furthermore, the field extends inside the cladding and the overlap integral Γ_{ov} accounts for it. Consequently, the expression of the field turns to be

$$r_1 E_0 exp\Big(- \frac{\alpha_{loss} L}{2} + \frac{g\Gamma_{ov} L}{2} + jk_x L\Big). \tag{37}$$

4. The effect of the reflection of the left-hand mirror can be expressed as

$$r_2 r_1 E_0 exp\Big(- \frac{\alpha_{loss} L}{2} + \frac{g\Gamma_{ov} L}{2} + jk_x L\Big). \tag{38}$$

5. When the wave reaches the final point both the amplitude and phase are further modified leading to

$$r_2 r_1 E_0 exp\Big(- \frac{\alpha_{loss} L}{2} \cdot 2 + \frac{g\Gamma_{ov} L}{2} \cdot 2 + jk_x L \cdot 2\Big). \tag{39}$$

The self-sustain condition is obtained by pretending to have the same amplitude and phase at the beginning and end of the round trip. This implies that the field in points 1 and 5 must be the same. For simplicity, if the mirrors have the same reflectivities ($r_1 = r_2 = r$ where $|r|^2 = R$) the round trip condition turns to be

$$E_0 = RE_0 exp\Big(- \alpha_{loss} L + g\Gamma_{ov} L), \tag{40}$$

since the phase $j2k_x L$ is an integer multiple of 2π it disappears. Thus, the condition can be rewritten as

$$1 = exp\Big(- \alpha_{loss} L + g\Gamma_{ov} L + logR\Big), \tag{41}$$

then defining the cavity threshold gain

$$g_{th}\Gamma_{ov} = \alpha_{loss} + \frac{1}{L} log \frac{1}{R} = \alpha_{loss} + \alpha_m = \alpha_{tot} \tag{42}$$

the threshold condition is obtained

$$g_{th}\Gamma_{ov} = \alpha_{tot}. \tag{43}$$

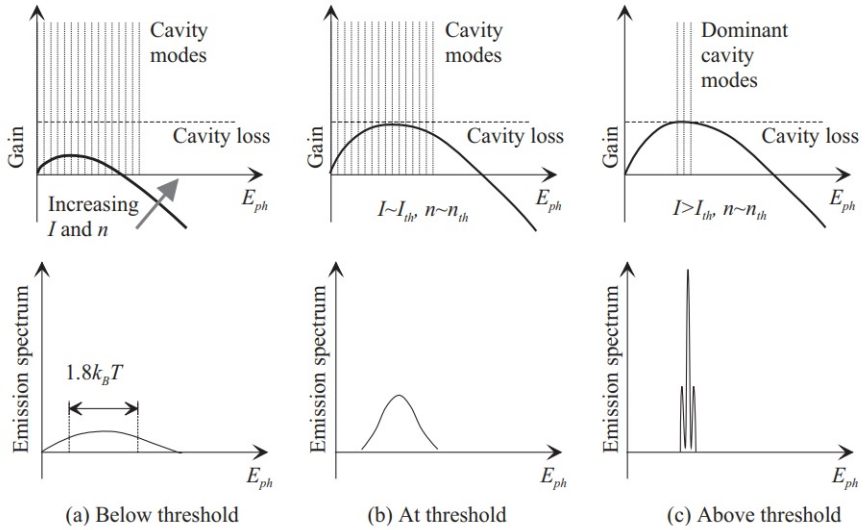

Figure 18: *Gain and emission spectrum as a function of photon energy in three cases: a) below the threshold by increasing the injected current, the photon density increases and the balance between gain and loss is not reached b) at the threshold the gain assesses the cavity loss and only certain cavity modes are allowed to propagate as it is shown in case c). Moreover, once the lasing is reached the spectrum is narrow and has high peak, differently from the broad and low spectrum below the threshold [58].*

Figure 18 illustrates the gain, cavity loss and modes for three different values of injected current. Below the threshold, the spontaneous emission predominates over the stimulated one and the laser works as a LED with a broad emission spectrum. If the current increases till the threshold, the gain compensates the cavity loss and cavity modes experience positive feedback from stimulated emission. This leads to a very narrow emission spectrum as shown in Figure 18 (c). Despite all, if the current increases above the threshold the gain is clamped: this is due to the reduction of stimulated lifetime induced by the higher output power.

Frequency-doubling

Frequency-doubling, known also as second harmonic generation, is a nonlinear optical process which allows the generation of an optical beam having the energy doubled compared to the input signal. This phenomenon is strictly related to the second order susceptibility $\chi^{(2)}$ and crystals without inversion center are required for the generation [60] - [61].
Nevertheless, the use of these crystals is not sufficient: the frequency-doubling is possible only if the condition of phase-matching is met. This means that the interacting waves must satisfy a proper relation during the propagation and, consequently, they will reach the end of the nonlinear crystal with the same phase. However, dispersion causes phase mismatch and, as known, cannot be avoided. For this reason, birefringence is used to delete the mismatch and achieve a good conversion efficient in the nonlinear medium.

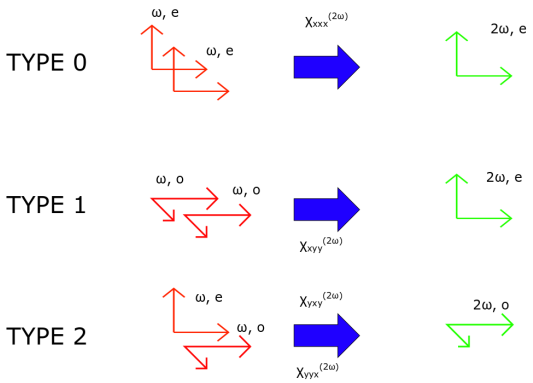

Figure 19: *Classification of critical phase-matching: the output polarization depends on both the impinging polarization and on the second order susceptibility tensor.*

There are different techniques according to the photons polarization and crystallographic orientation of the birefringent crystal. They are classified in critical

and noncritical phase matching. If the first is based on an angular adjustment of the crystal to find the matching configuration, the other does not depend on the angular position since all polarization directions are directed towards the crystal axes [62]. The critical phase matching includes three different cases, illustrated in Figure 19. Given a crystallographic orientation, only one of the following case occurs.

- **Type 0** All waves have the same polarization and birefringence is not involved. The two impinging photons with extraordinary polarization combine and generate the output photon characterized by doubled energy and extraordinary polarization.
- **Type I** The two beams with ordinary polarization generate a doubled-frequency photon with extraordinary polarization.
- **Type II** The two fundamental beams have different polarization directions and form one photon ordinary-polarized.

Under phase-matching condition, photons interacting with a nonlinear crystal allow the electron excitation to two consecutive virtual states. After the relaxation to the ground state, the emission of frequency-doubled photons is obtained, as represented in the sketch in Figure 20.

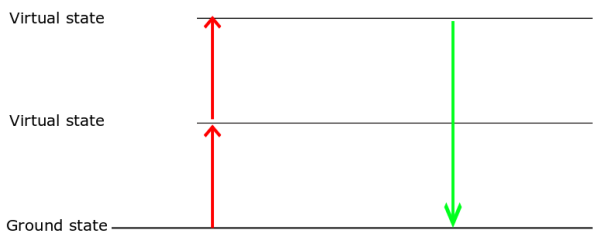

Figure 20: *Energy levels involved in SHG process.*

In the wave description, the incoming wave (pump signal) generates a nonlinear polarization after the interaction with the crystal. Thus, an electromagnetic wave with doubled oscillation frequency is generated according to Maxwell's equations, as described in Equation 44. Phase-matching allows its propagation in the direction of the nonlinear polarization wave.

$$E(2\omega) \approx P^{(2)}(2\omega) = \chi^{(2)} E(\omega) E(\omega). \tag{44}$$

Under low pump intensity conditions, the relation between the pump intensity and the second-harmonic has a square behaviour

$$I_2 = \gamma I_0^2, \tag{45}$$

where I_2 is the second-harmonics intensity, I_0 the pump intensity and the coefficient γ takes into account different factors which influence the generation, such as the effective mode area, the length of the crystal and many crystal properties including the effective nonlinearity [63].

The high sensibility to phase variation makes this process particularly hard to handle. However, if a high pump signal is combined with a good phase-matching, efficiency up to 80% is reached which leads to an output beam with good beam quality, high intensity and large optical bandwidth [64].

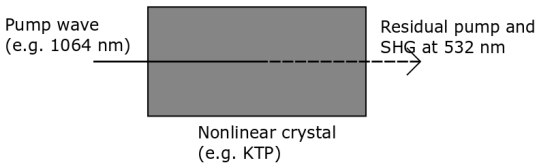

Figure 21: *Frequency-doubling using a KTP crystal.*

A simplified sketch of the SHG implemented in this work is shown in Figure 21. The pump signal at 1064 nm is launched into the KTP crystal. After the interaction the frequency is doubled (532 nm) and some residual pump signal is transmitted.
KTP crystal is greatly exploited in modulators and diode-pumped solid-state lasers for frequency-doubling [65]. In facts, thanks to its outstanding properties it turns to be the material of choice for both nonlinear optic and electro-optic applications.

In particular, it is widely used for frequency-doubling Nd:YAG lasers and other Nd-doped laser systems emitting near 1.06 μm [66]. Many studies have demonstrated its interesting and attractive characteristics, such as large electro-optic coefficient, low dielectric constant, low absorption, high acceptance angle and low bulk damage in resonant cavity [65].

Bibliography

[1] Steffen Novotny, Vasuki Durairaj, Igor Shavrin, Lauri Lipiäinen, Kimmo Kokkonen, Matti Kaivola, and Hanne Ludvigsen. «Picosecond supercontinuum light source for stroboscopic white-light interferometry with freely adjustable pulse repetition rate». In: *Optics express* 22.11 (2014), pp. 13625–13633 (cit. on pp. i, 1, 2, 49, 52, 69).

[2] Rüdiger Paschotta. «Understanding fiber amplifiers and lasers: Numerical modeling gives vital insights into the development of new designs». In: *Laser Technik Journal* 8.5 (2011), pp. 45–47 (cit. on p. 1).

[3] SB Poole, David N Payne, and M_E Fermann. «Fabrication of low-loss optical fibres containing rare-earth ions». In: *Electronics Letters* 21.17 (1985), pp. 737–738 (cit. on p. 1).

[4] RJ Mears, L Reekie, SB Poole, and DNs Payne. «Neodymium-doped silica single-mode fibre lasers». In: *Electronics letters* 21.17 (1985), pp. 738–740 (cit. on p. 1).

[5] Wei Shi, Qiang Fang, Xiushan Zhu, R. A. Norwood, and N. Peyghambarian. «Fiber lasers and their applications

Invited

». In: *Appl. Opt.* 53.28 (Oct. 2014), pp. 6554–6568. DOI: 10.1364/AO.53.006554. URL: http://ao.osa.org/abstract.cfm?URI=ao-53-28-6554 (cit. on p. 1).

[6] Govind P Agrawal. «Nonlinear fiber optics». In: *Nonlinear Science at the Dawn of the 21st Century*. Springer, 2000, pp. 195–211 (cit. on pp. 4, 7–12, 14, 70).

[7] R. Paschotta. «article on 'effective mode area' in the Encyclopedia of Laser Physics and Technology». In: (Oct. 2008) (cit. on p. 4).

[8] Linn F Mollenauer and James P Gordon. *Solitons in optical fibers: fundamentals and applications*. Elsevier, 2006 (cit. on p. 6).

[9] Govind P Agrawal. *Fiber-optic communication systems*. Vol. 222. John Wiley & Sons, 2012 (cit. on p. 8).

[10] Vincent Loriot, Edouard Hertz, Olivier Faucher, and Bruno Lavorel. «Measurement of high order Kerr refractive index of major air components». In: *Optics express* 17.16 (2009), pp. 13429–13434 (cit. on p. 9).

[11] Carsten Brée, Ayhan Demircan, and Günter Steinmeyer. «Saturation of the all-optical Kerr effect». In: *Physical review letters* 106.18 (2011), p. 183902 (cit. on p. 9).

[12] Bastian Borchers, Carsten Brée, Simon Birkholz, Ayhan Demircan, and Günter Steinmeyer. «Saturation of the all-optical Kerr effect in solids». In: *Optics letters* 37.9 (2012), pp. 1541–1543 (cit. on p. 9).

[13] Dan Grahelj and Igor Poberaj. «Solitons in optics». In: *Department of Physics, University of Ljubljana, Seminar*. 2010 (cit. on pp. 10, 11).

[14] DF Walls and GJ Milburn. «Quantum Optics Springer». In: *New York* (1994) (cit. on p. 12).

[15] John M Dudley, Goëry Genty, and Stéphane Coen. «Supercontinuum generation in photonic crystal fiber». In: *Reviews of modern physics* 78.4 (2006), p. 1135 (cit. on p. 12).

[16] RH Stolen and EP Ippen. «Raman gain in glass optical waveguides». In: *Applied Physics Letters* 22.6 (1973), pp. 276–278 (cit. on p. 17).

[17] RW Tkach, AR Chraplyvy, and RM Derosier. «Spontaneous Brillouin scattering for single-mode optical-fibre characterisation». In: *Electronics Letters* 22.19 (1986), pp. 1011–1013 (cit. on p. 18).

[18] Fedor Mitschke and Fedor Mitschke. *Fiber Optics*. Springer, 2016 (cit. on pp. 21, 22).

[19] Tim A Birks, Jonathan C Knight, and P St J Russell. «Endlessly single-mode photonic crystal fiber». In: *Optics letters* 22.13 (1997), pp. 961–963 (cit. on p. 21).

[20] Philip Russell. «Photonic crystal fibers». In: *science* 299.5605 (2003), pp. 358–362 (cit. on p. 21).

[21] RR Alfano. *The supercontinuum laser source: fundamentals with updated references, 2006* (cit. on p. 21).

[22] JC Knight, J Arriaga, TA Birks, A Ortigosa-Blanch, WJ Wadsworth, and P St J Russell. «Anomalous dispersion in photonic crystal fiber». In: *IEEE photonics technology letters* 12.7 (2000), pp. 807–809 (cit. on p. 22).

[23] R. Paschotta. «article on 'supercontinuum generation' in the Encyclopedia of Laser Physics and Technology». In: (Oct. 2008) (cit. on p. 23).

[24] John M Dudley, Laurent Provino, Nicolas Grossard, Hervé Maillotte, Robert S Windeler, Benjamin J Eggleton, and Stéphane Coen. «Supercontinuum generation in air–silica microstructured fibers with nanosecond and femtosecond pulse pumping». In: *JOSA B* 19.4 (2002), pp. 765–771 (cit. on pp. 24, 25).

[25] Stephane Coen, Alvin Hing Lun Chau, Rainer Leonhardt, John D Harvey, Jonathan C Knight, William J Wadsworth, and Philip St J Russell. «White-light supercontinuum generation with 60-ps pump pulses in a photonic crystal fiber». In: *Optics letters* 26.17 (2001), pp. 1356–1358 (cit. on p. 24).

[26] Goëry Genty, M Lehtonen, H Ludvigsen, J Broeng, and M Kaivola. «Spectral broadening of femtosecond pulses into continuum radiation in microstructured fibers». In: *Optics Express* 10.20 (2002), pp. 1083–1098 (cit. on pp. 25–27).

[27] Jianlong Yang, Yulong Tang, and Jianqiu Xu. «Development and applications of gain-switched fiber lasers». In: *Photonics Research* 1.1 (2013), pp. 52–57 (cit. on pp. 28, 30, 31).

[28] R. Paschotta. «article on 'Q switching' in the Encyclopedia of Laser Physics and Technology». In: (Oct. 2008) (cit. on p. 29).

[29] Andreas Tünnermann, Thomas Schreiber, and Jens Limpert. «Fiber lasers and amplifiers: an ultrafast performance evolution». In: *Applied optics* 49.25 (2010), F71–F78 (cit. on pp. 31, 58).

[30] R. Paschotta. «article on 'Quantum defects' in the Encyclopedia of Laser Physics and Technology». In: (Oct. 2008) (cit. on p. 31).

[31] Davis J Richardson, J Nilsson, and WA Clarkson. «High power fiber lasers: current status and future perspectives». In: *JOSA B* 27.11 (2010), B63–B92 (cit. on pp. 31, 58).

[32] Wei Shi, Qiang Fang, Xiushan Zhu, Robert A Norwood, and N Peyghambarian. «Fiber lasers and their applications». In: *Applied optics* 53.28 (2014), pp. 6554–6568 (cit. on pp. 32, 58).

[33] Qiang Fang, Wei Shi, Khanh Kieu, Eliot Petersen, Arturo Chavez-Pirson, and Nasser Peyghambarian. «High power and high energy monolithic single frequency 2 μm nanosecond pulsed fiber laser by using large core Tm-doped germanate fibers: experiment and modeling». In: *Optics Express* 20.15 (2012), pp. 16410–16420 (cit. on pp. 32, 58).

[34] E Snitzer. «Proposed fiber cavities for optical masers». In: *Journal of Applied Physics* 32.1 (1961), pp. 36–39 (cit. on p. 33).

[35] S. M. M. Ali et al. «Comparison of linear and ring lasers of thulium-ytterbium co-doped fiber». In: *2012 International Conference on Computer and Communication Engineering (ICCCE)*. 2012, pp. 621–624 (cit. on p. 33).

[36] E Snitzer, H Po, F Hakimi, R Tumminelli, and BC McCollum. «Double clad, offset core Nd fiber laser». In: *Optical fiber sensors*. Optical Society of America. 1988, PD5 (cit. on p. 34).

[37] Stuart D Jackson. «Towards high-power mid-infrared emission from a fibre laser». In: *Nature photonics* 6.7 (2012), p. 423 (cit. on p. 35).

[38] Rudiger Paschotta, Johan Nilsson, Anne C Tropper, and David C Hanna. «Ytterbium-doped fiber amplifiers». In: *IEEE Journal of quantum electronics* 33.7 (1997), pp. 1049–1056 (cit. on p. 35).

[39] COMSOL AB. *COMSOL Multiphysics*®. Version 5.4. Stockholm, Sweden. URL: https://comsol.com (cit. on pp. 39, 64).

[40] James W Fleming. «Dispersion in GeO 2–SiO 2 glasses». In: *Applied Optics* 23.24 (1984), pp. 4486–4493 (cit. on p. 40).

[41] Anders Bjarklev, Jes Broeng, and Araceli Sanchez Bjarklev. *Photonic crystal fibres*. Springer Science & Business Media, 2012 (cit. on p. 40).

[42] *MATLAB R2018b*. The Mathworks, Inc. Natick, Massachusetts, 2018 (cit. on p. 40).

[43] Allen Taflove and Susan C Hagness. *Computational electrodynamics: the finite-difference time-domain method*. Artech house, 2005 (cit. on p. 41).

[44] Garland Best and Ömür M Sezerman. «Shedding light on hybrid optics: A tutorial in coupling». In: *Optics and Photonics News* 10.2 (1999), pp. 30–34 (cit. on pp. 45, 49, 52).

[45] RP Photonics. *RP Fiber Power*®. Version 5.0. URL: https://www.rp-photonics.com/ (cit. on p. 47).

[46] CD Hussey and F Martinez. «Approximate analytic forms for the propagation characteristics of single-mode optical fibres». In: *Electronics Letters* 21.23 (1985), pp. 1103–1104 (cit. on p. 48).

[47] Jay Dawson et al. «Analysis of the Scalability of Diffraction-Limited Fiber Lasers and Amplifiers to High Average Power». In: *Optics express* 16 (Sept. 2008), pp. 13240–66. DOI: 10.1364/OE.16.013240 (cit. on p. 49).

[48] *OceanInsight*®. URL: https://www.oceaninsight.com/ (cit. on p. 58).

[49] Morris Engelson and Len Garrett. «The pulse desensitization factor». In: *Microwave Journal* 41.3 (1998), pp. 118–122 (cit. on p. 58).

[50] Javier Alda. «Laser and Gaussian beam propagation and transformation». In: *Encyclopedia of optical engineering* 2013 (2003), pp. 999–1013 (cit. on p. 60).

[51] Sidney A Self. «Focusing of spherical Gaussian beams». In: *Applied optics* 22.5 (1983), pp. 658–661 (cit. on p. 60).

[52] Ophir-Spiricon Laser Beam Profilers. *BeamStar FX 110* (cit. on p. 62).

[53] Bahaa EA Saleh and Malvin Carl Teich. *Fundamentals of photonics*. john Wiley & sons, 2019 (cit. on p. 65).

[54] John M Dudley and James Roy Taylor. *Supercontinuum generation in optical fibers*. Cambridge University Press, 2010 (cit. on p. 67).

[55] Vasuki Durairaj, Iván Bravo Gonzalo, Steffen Novotny, and Hanne Ludvigsen. «Picosecond supercontinuum generation: Numerical and experimental analysis». English. In: *Northern Optics and Photonics (NOP 2015), 2-4 June 2015, Lappeenranta, Finland*. 2015. ISBN: 978-952-61-1751-5 (cit. on pp. 67, 69).

[56] John M. Dudley, Laurent Provino, Nicolas Grossard, Hervé Maillotte, Robert S. Windeler, Benjamin J. Eggleton, and Stéphane Coen. «Supercontinuum generation in air–silica microstructured fibers with nanosecond and femtosecond pulse pumping». In: *J. Opt. Soc. Am. B* 19.4 (Apr. 2002), pp. 765–771 (cit. on p. 69).

[57] E Räikkönen, G Genty, O Kimmelma, M Kaivola, KP Hansen, and SC Buchter. «Supercontinuum generation by nanosecond dual-wavelength pumping in microstructured optical fibers». In: *Optics express* 14.17 (2006), pp. 7914–7923 (cit. on p. 70).

[58] Giovanni Ghione. *Semiconductor devices for high-speed optoelectronics*. Vol. 116. Cambridge University Press Cambridge, 2009 (cit. on pp. 75, 79).

[59] Larry A Coldren, Scott W Corzine, and Milan L Mashanovitch. *Diode lasers and photonic integrated circuits*. Vol. 218. John Wiley & Sons, 2012 (cit. on p. 77).

[60] KD SINGER, Y WU, and Case Western. «Second harmonic generation (SHG) as a characterization technique and phenomological probe for organic materials». In: *Handbook of Organic Materials for Optical and (Opto) Electronic Devices: Properties and Applications* (2013), p. 442 (cit. on p. 80).

[61] AD Li and WC Liu. «Optical properties of ferroelectric nanocrystal/polymer composites». In: *Physical Properties and Applications of Polymer Nanocomposites*. Elsevier, 2010, pp. 108–158 (cit. on p. 80).

[62] R. Paschotta. «article on 'f'phase matching" in the Encyclopedia of Laser Physics and Technology». In: (Oct. 2008) (cit. on p. 81).

[63] R. Paschotta. «article on 'frequency doubling' in the Encyclopedia of Laser Physics and Technology». In: (Oct. 2008) (cit. on p. 82).

[64] R Paschotta, P Kürz, R Henking, S Schiller, and J Mlynek. «82% efficient continuous-wave frequency doubling of 1.06 μm with a monolithic MgO: LiNbO 3 resonator». In: *Optics Letters* 19.17 (1994), pp. 1325–1327 (cit. on p. 82).

[65] John D Bierlein and Herman Vanherzeele. «Potassium titanyl phosphate: properties and new applications». In: *JOSA B* 6.4 (1989), pp. 622–633 (cit. on p. 82).

[66] RF Belt, G Gashurov, and YS Liu. «KTP as a harmonic generator for Nd: YAG lasers». In: *Laser focus (1983)* 21.10 (1985), pp. 110–124 (cit. on p. 82).